







Article

# Monitoring forest health using hyperspectral imagery: Does feature selection improve the performance of machine-learning techniques?

Patrick Schratz <sup>1</sup> , Jannes Muenchow <sup>1</sup> , Eugenia Iturritxa <sup>2</sup> , José Cortés <sup>1</sup> , Bernd Bischl <sup>3</sup>  and Alexander Brenning <sup>1</sup> 

<sup>1</sup> Friedrich Schiller University Jena, Department of Geography, GIScience group, Germany

<sup>2</sup> NEIKER Tecnalia, Spain

<sup>3</sup> Ludwig-Maximilians-University Munich, Department of Statistics, Computational Statistics group, Germany

\* Correspondence: patrick.schratz@uni-jena.de

**Abstract:** This study analyzed highly-correlated, feature-rich datasets from hyperspectral remote sensing data using multiple machine and statistical-learning methods. The effect of filter-based feature-selection methods on predictive performance was compared. Also, the effect of multiple expert-based and data-driven feature sets, derived from the reflectance data, was investigated. Defoliation of trees (%), derived from in-situ measurements in fall 2016, was modeled as a function of reflectance. Variable importance was assessed using permutation-based feature importance. Overall support vector machine (SVM) outperformed other algorithms such as random forest (RF), extreme gradient boosting (XGBoost), lasso (L1) and ridge (L2) regression by at least three percentage points. The combination of certain feature sets showed small increases in predictive performance while no substantial differences between individual feature sets were observed. For some combinations of learners and feature sets, filter methods achieved better predictive performances than using no feature selection. Ensemble filters did not have a substantial impact on performance. Permutation-based feature importance estimated features around the red edge to be most important. However, the presence of features in the near-infrared region (800 nm - 1000 nm) was essential to achieve the overall best performances. More training data and replication in similar benchmarking studies is needed for more generalizable conclusions. Filter methods have the potential to be helpful in high-dimensional situations and are able to improve the interpretation of feature effects in fitted models, which is an essential constraint in environmental modeling studies.

**Keywords:** hyperspectral imagery; forest health monitoring; machine learning; feature selection; model comparison

**Citation:** Schratz, P.; Muenchow, J.; Cortés, J.; Iturritxa, E.; Bischl, B.; Brenning, A. Title. *Remote Sens.* **2021**, *1*, 0. <https://doi.org/>

Received:

Accepted:

Published:

**Publisher's Note:** MDPI stays neutral with regard to jurisdictional claims in published maps and institutional affiliations.

**Copyright:** © 2021 by the authors. Submitted to *Remote Sens.* for possible open access publication under the terms and conditions of the Creative Commons Attribution (CC BY) license (<https://creativecommons.org/licenses/by/4.0/>).

## 1. Introduction

The use of machine learning (ML) algorithms for analyzing remote sensing data has seen a huge increase in the last decade [1]. This coincided with the increased availability of remote sensing imagery, especially since the launch of the first Sentinel satellite in the year 2014, which serves as training and prediction data. At the same time, the implementation and usability of learning algorithms has been greatly simplified with many contributions from the open-source community. Scientists can nowadays process large amounts of (environmental) information with relative ease using various learning algorithms. This makes it possible to easily extend benchmark comparison matrices of studies in a semi-automated way, possibly stumbling across unexpected findings of process settings that would not have been explored otherwise [2].

ML methods in combination with remote sensing data are used in many environmental fields such as vegetation cover analysis or forest carbon storage mapping [3,4].

The ability of predicting into unknown space qualifies ML algorithms as a helpful tool for such environmental analyses. One aspect of this research field is to enhance the understanding of biotic and abiotic stress triggers, for example by analyzing tree defoliation [5]. Defoliation is known to be a proxy for pathogen and insect damage [6]. While common symptoms are observable across species, some effects and their degree are species-specific [7]. Defoliation has also been shown to increase predisposition of tree death from secondary biotic factors of up to ten years after the actual defoliation event [8]. Other approaches for analyzing forest health include change detection [9] or describing the current health status of forests on a stand level [10].

Vegetation indices have shown the potential to provide valuable information when analyzing forest health [11,12]. Most vegetation indices were developed with the aim of being sensitive to changes of specific wavelength regions, serving as a proxy for underlying plant processes. However, indices developed/applied for different purposes than the one to be analyzed (i.e. defoliation at pine trees) may help to explain complex underlying relationships which are not obvious at first. This emphasizes the need to extract as much information as possible from the available input data to generate promising features which can help to understand the modeled relationship [13]. A less known index type which can be derived from spectral information is the normalized ratio index (NRI). In contrast to most vegetation indices, NRIs do not use an expert-based formula following environmental heuristics but instead makes use of a data-driven feature engineering approach by combining (all possible) combinations of spectral bands [14]. When working with hyperspectral data, thousands of NRI features can be derived this way.

Even though ML algorithms are capable of handling highly correlated input variables, model fitting becomes computationally more demanding, and model interpretation more complex. Feature selection approaches can help to address this issue, reducing possible noise in the feature space, simplify model interpretability and possibly enhance predictive performance [15]. Instead of using wrapper feature selection methods, which add a substantial overhead to a nested model optimization approach, especially for datasets with many features, this study focuses on the use of (ensemble) filter methods which can be directly integrated into the hyperparameter optimization step during model creation.

Overall, this study aims to show how high-dimensional datasets can be handled effectively with ML methods while still being able to interpret the fitted models. The predictive power of non-linear methods and their ability to handle highly correlated predictors is combined with common and new approaches for assessing feature importance and feature effects. Yet, this study focuses on investigating the effects of filter methods and feature set types on predictive performance rather than interpreting individual feature effects.

Considering these opportunities and challenges, the research questions of this study are the following:

- Do different (environmental) feature sets show differences in performance when modeling defoliation of trees?
- Can predictive performance be substantially improved by combining feature sets?
- How do different feature selection methods influence the predictive performance of the models?
- Which features are most important and how can these be interpreted in an environmental context?

Despite their popularity in environmental modeling, there are no studies so far which used ML algorithms in combination with remote sensing data to analyze defoliation at the tree level. This study aims to close this gap by analyzing tree defoliation in northern Spain using airborne hyperspectral data. The methodology of this study uses ML methods in combination with feature selection and hyperparameter tuning. In addition, feature importance was analyzed. Incorporating the idea of creating data-driven NRIs, this study also discusses the practical problems of high dimensionality in environmental modeling [16,17].

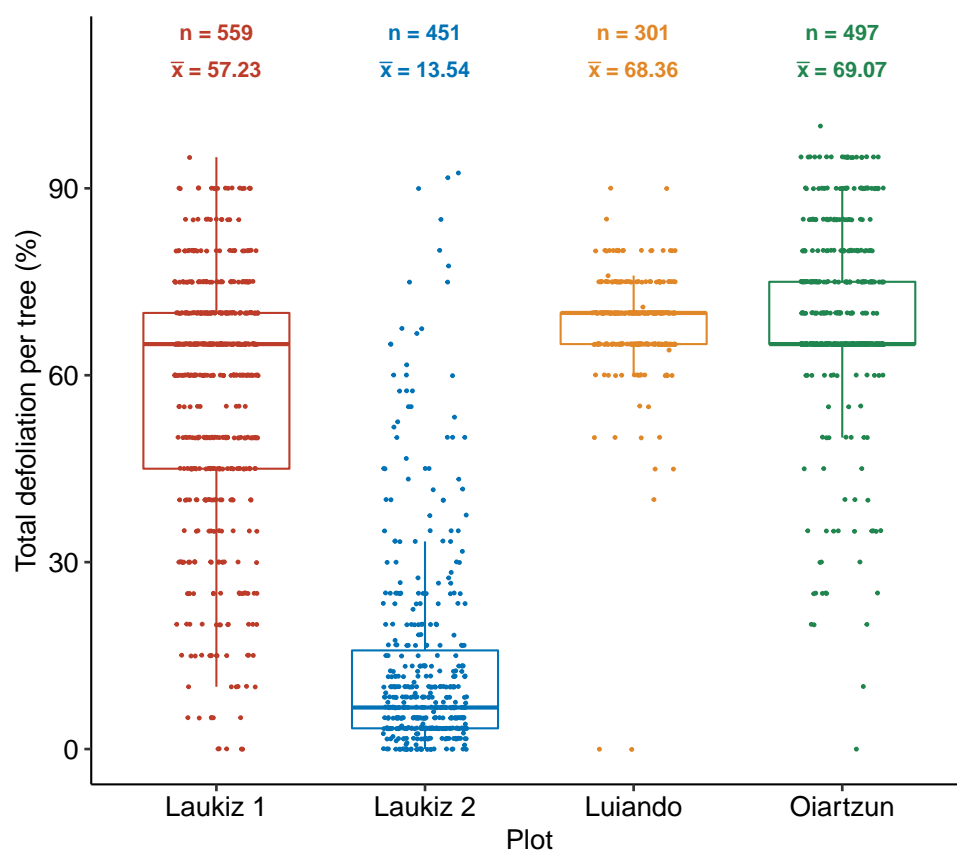


**Figure 1.** Response variable "defoliation at trees" for plots Laukiz1, Laukiz2, Luiando and Oiartzun.  $n$  corresponds to the total number of trees in the plot,  $\bar{x}$  refers to the mean defoliation, respectively. Values for Laukiz1, Luiando and Oiartzun were observed in 5% intervals; for Laukiz2 defoliation was observed at multiple heights and then averaged, leading to smaller defoliation differences than 5%.

## 2. Materials and Methods

### 2.1. Data and study area

Airborne hyperspectral data with a spatial resolution of one meter and 126 spectral bands was available for four Monterey Pine (*Pinus radiata* D. Don) plantations in northern Spain. The trees in the plots suffer from infections of pathogens such as *Diplodia sapinea* (Fr.) Fuckel, *Fusarium circinatum* Nirenberg & O'Donnell, *Armillaria mellea* (Vahl) P. Kumm, *Heterobasidion annosum* (Fr.) Bref, *Lecanosticta acicola* (Thüm) Syd. and *Dothistroma septosporum* (Dorogin) M. Morelet causing (among others) needle blight, pitch canker and root diseases [18,19]. The first two fungi are mainly responsible for the foliage loss of the trees analyzed in this study [20]. In-situ measurements of defoliation of trees (serving as a proxy for tree health) were collected by visual inspection of experts in the field to serve as the response variable *defoliation* which ranges from 0 - 100 (in %) (Figure 1).

It is assumed that the fungi infect the trees through open wounds, possibly caused by previous hail damage [20]. The dieback of these trees, which are mainly used as timber, causes high economic damages [21].

#### 2.1.1. In-situ data

The *Pinus radiata* plots of this study, namely Laukiz1, Laukiz2, Luiando and Oiartzun, are located in the northern part of the Basque Country (Figure 2). Oiartzun consists of most tree observations ( $n = 559$ ) while Laukiz2 shows the largest area size

Table 1: Specifications of hyperspectral data.

Characteristic	Value
Geometric resolution	1 m
Radiometric resolution	12 bit
Spectral resolution	126 bands (404.08 nm — 996.31 nm)
Correction:	Radiometric, geometric, atmospheric

(1.44 ha). All plots besides Luiando are located within 100 km from the coast (Figure 2). In total 1808 observations are available (Laukiz1 = 559, Laukiz2 = 451, Luiando = 301, Oiartzun = 497). Field surveys were conducted in September 2016 by experienced forest pathologists. Defoliation was measured via visual inspection using 5% intervals with the help of a dedicated score card. For Laukiz2, values at three height levels (bottom, mid, top) were available and averaged into an overall defoliation value, leading to values outside of the 5% interval of the other three plots (e.g. 8.33 %). Estimating the human observer error of such surveys when assessing defoliation is an issue which is being discussed since many years [22]. Even though no estimation error was recorded in this study, [23] estimated human observer errors when assessing defoliation to range between 7% - 18%.

### 2.1.2. Hyperspectral data

The airborne hyperspectral data was acquired during two flight campaigns which took place at noon on September 28th and October 5th 2016. Images were taken by an AISA EAGLE-II sensor. All preprocessing steps (geometric, radiometric, atmospheric) were conducted by the Institut Cartogràfic i Geològic de Catalunya (ICGC). The first four bands were corrupted, leaving 122 bands with valid information. Additional metadata information is available in Table 1.

### 2.2. Derivation of indices

To use the full potential of the hyperspectral data, all possible vegetation indices supported by the R package *hsdar* (89 in total) as well as all possible NRI combinations were calculated. NRIs follow the optimized multiple narrow-band reflectance (OMNBR) concept of data-driven information extraction from narrow-band indices of hyperspectral data [13,14]. While various index formulations such as band ratios or normalized ratios are available, indices involving the same bands are strongly correlated. Since the widely-used NDVI index belongs to the family of normalized ratio indices (NRIs), which are implemented in the *hsdar* R package, we used the following normalized difference index (NDI) formula to combine all pairs of reflectances:

$$NRI_{i,j} = \frac{band_i - band_j}{band_i + band_j} \quad (1)$$

where  $i$  and  $j$  are the respective band numbers.

To account for geometric offsets within the hyperspectral data, which were reported to be potentially up to one meter from ICGC, a buffer of one meter around the centroid of each tree was used when extracting the reflectance values. A pixel was considered to fall into a tree's buffer zone if the centroid of the respective pixel was touched by the buffer. The pixel values of such were averaged and formed the final reflectance value of a single tree and were used as the base information to derive all additional feature sets. In total,  $\frac{121 \times 122}{2} = 7381$  NRIs were calculated.

### 2.3. Feature selection

High-dimensional, feature-rich datasets come with several challenges for both model fitting and evaluation.



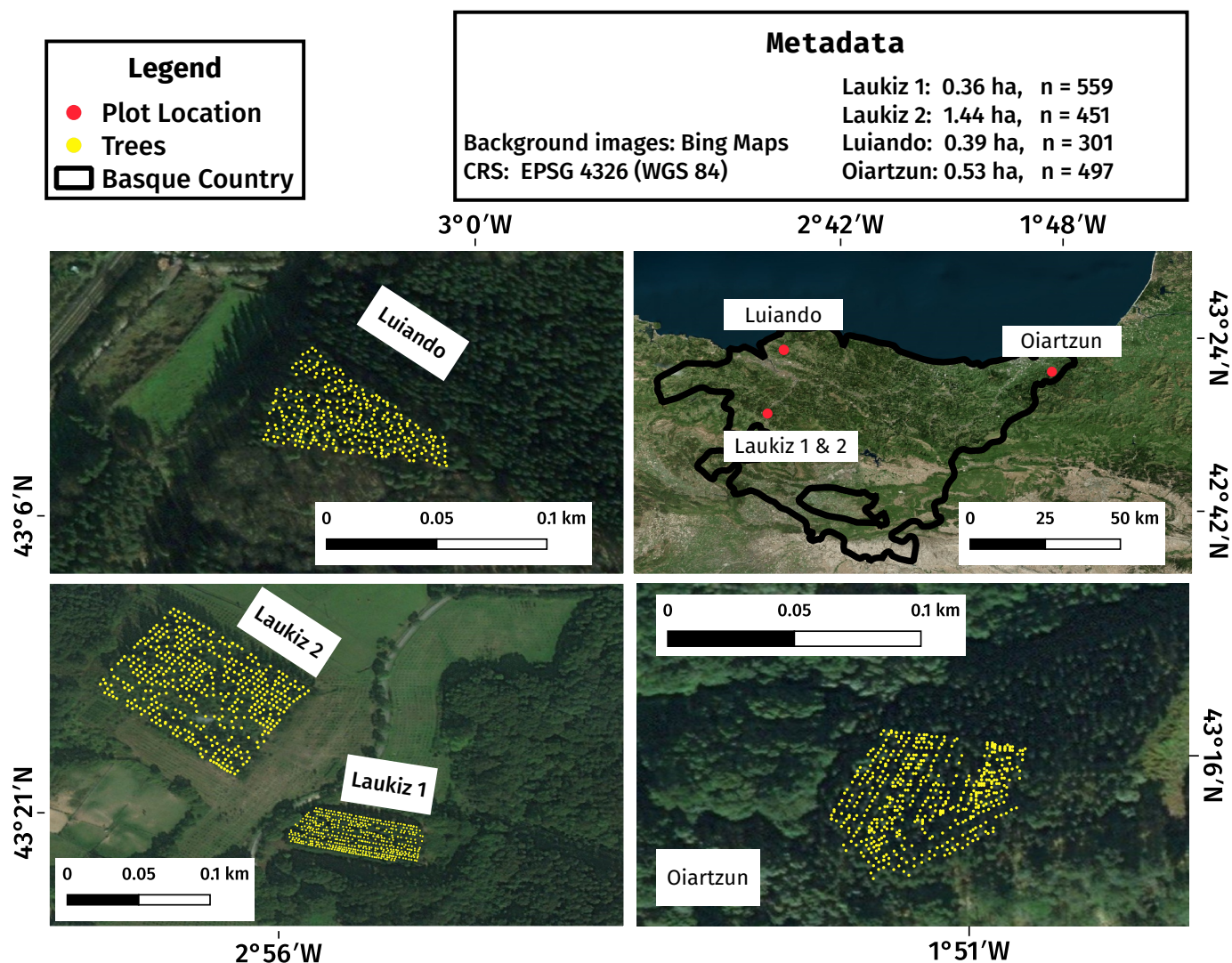


**Figure 2.** Study area maps showing information about location, size and spatial distribution of trees for all plots (Laukiz1, Laukiz2, Luiando, Oiartzun). The background maps used should give a visual impression of the individual plot area but do not necessarily represent the plot state during data acquisition.

- Model fitting times increase.
- Noise is possibly introduced into models by highly correlated variables [24].
- Model interpretation and prediction become more challenging [24].

To reduce the feature space of a dataset, conceptually differing approaches exist: wrapper methods, filters, penalization methods (lasso and ridge) or principal component analysis (PCA) [25–28]. In contrast to wrapper methods, filters can be added to the hyperparameter optimization step and have a lower computational footprint. In addition, filters are less known than wrapper methods and in recent years ensemble filters were introduced which have shown promising results compared to single filter algorithms [29]. These two points mainly led to the decision to focus on filter methods for this work and evaluate their effectiveness on highly-correlated, high-dimensional datasets. Due to this focus, only this sub-group of feature selection methods will be introduced in greater detail in the following sections.

### 160 2.3.1. Filter methods

161 The concept of filters originates from the idea of ranking features following a score  
 162 calculated by an algorithm [27]. Some filter methods can only deal with specific types  
 163 of variables (e.g. numeric or nominal). Filters only rank features, they do not decide  
 164 which covariates to drop or keep [30]. The selection which features to keep for model  
 165 fitting is usually done within the optimization phase during model fitting, along with the  
 166 hyperparameter tuning. Essentially, the number of covariates in the model is treated as  
 167 a additional hyperparameter of the model. The idea is to optimize the number of ranked  
 168 features to the point at which the model achieves the best performance.

169 Besides the concept of choosing a specific filter method to rank variables, studies  
 170 showed that combining several filters using statistical operations such as 'minimum' or  
 171 'mean' can possibly enhance the predictive performance of the resulting models, especially  
 172 when applied to multiple datasets [29,31]. This approach is referred to as 'ensemble  
 173 filtering' [32]. Ensemble filters align with the recent rise of the 'ensemble' approach in  
 174 ML which uses the idea of stacking to combine the predictions of multiple models, aiming  
 175 to enhance predictive performance [33–35]. In this work the 'Borda' ensemble filter was  
 176 used [29]. Its final feature order is determined by the sum of all single filters ranks.

177 Filter methods can be grouped into groups which are formed out of three binary  
 178 classes: multivariate or univariate feature use, correlation or entropy-based importance  
 179 weighting and linear and non-linear filter methodology. Care needs to be taken to not  
 180 weigh certain classes more than others in the ensemble as otherwise the final ranking  
 181 result will be biased. In this study this was taken care of by checking the rank correlations  
 182 (Spearman's correlation) of the generated feature rankings of all methods against each  
 183 other. If filter pairs showed a correlation of 0.9 or higher, only one of the two was  
 184 included into the ensemble filter, selected at random. This ensured that the ensemble  
 185 filter composition was not biased towards a certain group of filter methods.

### 186 2.3.2. Description of used filter methods

187 Filter methods can be classified as follows (Table 2):

- 188 • Univariate/multivariate (scoring based on a single variable / multiple variables).
- 189 • Linear/non-linear (usage of linear/non-linear calculations).
- 190 • Entropy/correlation (scoring based on derivations of entropy or correlation-based  
 191 approaches).

192 The filter 'Information Gain' is only defined for nominal response variables:

$$H(Class) + H(Attribute) - H(Class, Attribute) \quad (2)$$

193 where  $H$  is the conditional entropy of the response variable (class or  $Y$ ) or the  
 194 feature (attribute or  $X$ ), respectively.  $H(X)$  is Shannon's Entropy [42] for a variable  $X$   
 195 and  $H(X, Y)$  is a joint Shannon's Entropy for a variable  $X$  with a condition to  $Y$ .  $H(X)$   
 196 itself is defined as

Table 2: List of filter methods used in this work, their categorization and scientific reference.

Name	Group	Ref.
Linear correlation (Pearson)	univariate, linear, correlation	[36]
Information gain	univariate, non-linear, entropy	[37]
Minimum redundancy, maximum relevance	multivariate, non-linear, entropy	[38]
Carscore	multivariate, linear, correlation	[39]
Relief	multivariate, linear, entropy	[40]
Conditional minimal information maximization	multivariate, linear, entropy	[41]

$$H(X) = - \sum_{i=1}^n P(x_i) \log_b P(x_i) \quad (3)$$

where  $b$  is the base of the logarithm used (with  $b$  commonly being set to 2).  
In order to use this method with a numeric response (percentage defoliation of trees),  
the variable was discretized into equal bins  $n_{bin} = 10$  and treated as a class variable.

## 2.4. Benchmarking design

### 2.4.1. Algorithms

The following learners were used in this work:

- Extreme Gradient Boosting (XGBoost)
- Random Forest (RF)
- Penalized Regression (L1 (lasso) and L2 (ridge))
- Support Vector Machine (SVM, RBF Kernel)
- Featureless learner

RF and SVM are well established algorithms and widely used in (environmental) remote sensing. Extreme Gradient Boosting (commonly abbreviated as XGBoost) has shown promising results in benchmark studies in recent years. Penalized regression is a statistical modeling technique capable of dealing with highly-correlated covariates by penalizing the coefficients of the model [43]. Common penalties are 'lasso' (L1) and 'ridge' (L2). Ridge does not remove variables from the model (penalization to zero) but just shrinks them to effectively zero, keeping them in the model. A featureless learner was included for a baseline comparison.

In total the benchmarking grid consisted of 156 experiments (6 feature sets  $\times$  3 ML algorithms  $\times$  8 feature-selection methods and for the L1/L2 models, 6 feature sets  $\times$  2 models). The selected hyperparameter settings are shown in appendix Table 8. In addition code and data are available in the research compendium of this study (<https://doi.org/10.5281/zenodo.2635403>) to support open and reproducible science.

### 2.4.2. Feature sets

Three feature sets were used in this study, each representing a different approach to feature engineering:

- The raw hyperspectral band information (HR): no feature engineering)
- Vegetation Indices (vegetation index (VI)s): expert-based feature engineering)
- Normalized Ratio Indices (NRIs): data-driven feature engineering)

The idea of splitting the features into different sets originated from the question whether feature-engineered indices derived from reflectance values have a positive effect on model performance. Peña et al. 2017 [44] is an exemplary study which used this approach in a spectro-temporal setting. Benchmarking learners on these feature sets while keeping all other variables such as model type, tuning strategy and partitioning method constant makes it possible to draw conclusions on their individual impact. Each feature set has distinct capabilities which differentiate them from the others. This can have both a positive and negative effect on the resulting performance which is one item this study aims to explore. For example, feature set VI misses certain parts of the spectral range as the defined indices only cover parts of such. Feature set NRI will introduce highly-correlated features which might cause issues for some algorithms. However, rather than only looking at these three groups, also the following combinations of such were taken into account:

- HR + VI
- HR + NRI
- HR + VI + NRI

Some individual features of such were removed before using the datasets for modelling when being numerically equivalent to another feature based on the pairwise correlation being greater than  $1 - 10^{-10}$ . This preprocessing step reduced the number of covariates for feature set VI to 86 (from 89). This decision was made to prevent issues for the subsequent tuning, filtering and model fitting steps which might occur when passing features with a pairwise correlation of (almost) one. Additional variable selection was solely devoted to the respective feature selection methods in this study.

#### 2.4.3. Hyperparameter Optimization

Hyperparameters were tuned using model-based optimization (MBO) within a nested spatial cross-validation (CV) [45–47]. In MBO first  $n$  randomly chosen hyperparameter settings out of a user defined search space are composed. After these  $n$  settings have been evaluated, one new setting, which is going to be evaluated next, is proposed by a fitted surrogate model (by default a kriging method). This strategy continues until a termination criterion, defined by the user, is reached [48,49].

In this work, an initial design of 30 randomly composed hyperparameter settings in combination with a termination criterion of 70 iterations was used, resulting in a total budget of 100 evaluated hyperparameter settings per fold. The advantage of this tuning approach is a substantial reduction of the tuning budget that is required to find a setting close to the global optimization minimum. MBO may outperform methods that do not use information from previous iterations, such as random search or grid search [50]. Tuning ranges used in this work are shown in Table 8.

To optimize the number of features used for model fitting, the percentage of features was added as a hyperparameter during the optimization stage [46]. For PCA, the number of principal components was tuned. The RF hyperparameter  $m_{try}$  was re-expressed as  $m_{try} = p_{sel}^t$ , a function of the number of selected features,  $p_{sel}$ . It was thus tuned on a logarithmic scale by varying  $t$  between 0 (i.e.  $m_{try} = 1$ ) and 0.5 (i.e.  $m_{try} = \sqrt{p_{sel}}$ ). This was necessary to ensure that  $m_{try}$  was not chosen higher than the available number of features that were left after optimizing the feature percentage during tuning.

#### 2.4.4. Spatial resampling

A spatial nested cross-validation on the plot level was chosen to reduce the influence of spatial autocorrelation as much as possible [47,51]. The root mean square error (RMSE) was chosen as the error measure. Each plot served as one fold within the cross-validation setting, resulting in four iterations in total. For the inner level (hyperparameter tuning),  $k - 1$  folds were used with  $k$  being the number of plots.

### 2.5. Feature importance and feature effects

Estimating feature importance for datasets with highly correlated features is a complicated task for which many different approaches, model-specific and agnostic, exist [43,52,53]. The correlation between covariates makes it challenging to calculate an unbiased estimate for single features [54]. Methods like partial dependence plots (PDP) or permutation-based approaches may produce unreliable estimates in such scenarios because unrealistic situations between covariates are created [54]. The development of robust methods which enable an unbiased estimation of feature importance for highly correlated variables are subject to current research.

In this work permutation-based feature importance was calculated to estimate feature importance / effects [55]. With the limitations in mind when applied to correlated features, the aim was to get a general overview of the feature importance of the hyperspectral bands while trying to avoid an over-interpretation of results. The best-performing algorithm on the HR task (i.e. SVM) was used for the feature importance calculation.



## 2.6. Linking feature importance to wavelength regions

For environmental interpretation purposes the ten most important indices of the best performing models of feature sets HR and VI were linked to the spectral regions of the hyperspectral data. The aim was to visualize the most important features along the spectral curve of the plots to better understand which spectral regions were most important for the model.

## 2.7. Research compendium

All tasks of this study were conducted using the open-source statistical programming language R [56]. A complete list of all R packages used in this study can be found in the linked repositories mentioned in the next paragraph. Due to space limitations only the selected packages with high impact on this work will be explicitly cited.

The algorithm implementations of the following packages have been used: xgboost [57] (*Extreme Gradient Boosting*), kernlab [58] (Support Vector Machine) and glmnet [59] (penalized regression). The filter implementations of the following packages have been used: praznik [60], FSelectorRcpp [61]. Package mlr [62] was used for all modeling related steps. drake [63] was used for structuring the work and reproducibility. This study is available as a research compendium on Zenodo (10.5281/zenodo.2635403). Besides the availability of code and manuscript sources, a static webpage is available at (<https://pat-s.github.io/2019-feature-selection>), listing more side-analyses that were carried out during the creation of this study.

## 3. Results

### 3.1. PCA-based variance analysis of feature sets

PCA was used to assess the complexity of the three feature sets. Depending on the feature set, 95% of the variance is explained by two (HR), twelve (VI) and 42 (NRI) principal component (PC)s. HR features are therefore highly redundant, while the applied feature transformations enrich the data set, at least from an exploratory linear perspective.

### 3.2. Predictive performance

Overall, the response variable “tree defoliation” could be modeled with an RMSE of 28 percentage points (p.p.) (Figure 3). SVM showed almost no differences in RMSE across feature sets whereas other learners (RF, SVM, XGBoost, lasso and ridge) differed up to five p.p. (Figure 3). SVM showed the best overall performance with a mean difference of around three p.p. to the next best model (XGBoost) (Table 5). Performance differences between test folds were large: Predicting on Luiando resulted in an RMSE of 9.0 p.p. for learner SVM (without filter) but up to 54.3 p.p. when testing on Laukiz2 (Table 6).

The combination of feature sets showed small increases in performance for some learners. RF and XGBoost scored slightly better on the combined datasets HR-NRI, NRI-VI and HR-NRI-VI, respectively, compared to their standalone variants (NRI, VI) (Figure 3). However, the best performances for both RF and XGBoost were scored on HR only. Datasets containing derived features only (VI, NRI) showed no improvement in performance compared to the raw hyperspectral band information (HR) or combined feature sets.

SVM combined with the “Relief” filter achieved the best overall performance (RMSE of 28.09 p.p.) (Table 3). Regression with ridge (L2) and lasso (L1) penalty showed their best performances on the NRI feature set (Table 5). Difference to other feature sets were very small for lasso (below one p.p.) and a bit higher for ridge (between two and five p.p. (VI)). XGBoost shows bad performances for some feature sets and fills the ten last places of the ranking (Table 4). Especially when combined with PCA, the algorithm was not able to achieve adequate performances.

Effects of filter methods on performance differed greatly between algorithms: SVM showed no variation in performance across filters (Figure 4). Using filters for RF showed a substantial increase in performance for all tasks with the exception of NRI, for which the difference among all filters was also the smallest (Figure 4). XGBoost showed a high dependency on filtering the data: In two out of six tasks using no filter resulted in the worst or second worst performance. XGBoost shows the highest overall differences between filters for a single task: for feature set HR, the range is up to 15 p.p. (“CMIM” vs. “no filter”) (Figure 4).

When comparing the usage of filters against using no filter at all, there were no instances where a model without filtering scored a better performance than the best filtered one (Figure 4). For SVM, all filters and “no filter” achieved roughly the same performance on all tasks.

The Borda filter achieved in only one instance (RF on HR-NRI-VI) the best performance among the used filters (Figure 5). For RF and XGBoost it most often ranked within the first 50% with respect to all filters of a specific task. For XGBoost on the NRI task, the Borda filter scored the second worst performance.

Large differences were observed between the numbers of features selected during tuning for the subsequent fitting process across each learner and plot. While for RF least features were selected when Luiando or Oiartzun were the test set ( $n = 1$ ), more than 90% of all features were used for test sets Laukiz1 and Laukiz2 (Table 7). RF and SVM used very few features only when Laukiz1 was the test set, (three and one, respectively) whereas this was the plot for which XGBoost used almost all features ( $n = 1226$ ). Overall, SVM used the least features across all plots among all learners, with 24% for test set Laukiz2 being the highest single plot value. In general every learner behaved quite differently for each plot and no overall pattern could be observed.

Table 3: Best ten results among all learner-task-filter combinations, sorted in decreasing order of RMSE (p.p.) and their respective standard error (SE).

	Task	Model	Filter	RMSE	SE
1	HR	SVM	Borda	28.119	19.123
2	HR	SVM	MRMR	28.119	19.123
3	HR	SVM	Pearson	28.119	19.123
4	HR	SVM	Relief	28.119	19.123
5	NRI-VI	SVM	Car	28.122	19.123
6	NRI-VI	SVM	CMIM	28.122	19.123
7	HR-NRI	SVM	CMIM	28.122	19.123
8	VI	SVM	Info Gain	28.122	19.123
9	VI	SVM	No Filter	28.122	19.123
10	NRI-VI	SVM	No Filter	28.122	19.123

Table 4: Worst ten results among all learner-task-filter combinations, sorted in decreasing order of RMSE (p.p.) and their respective standard error (SE).

	Task	Model	Filter	RMSE	SE
1	NRI	XGBoost	PCA	48.161	9.161
2	NRI-VI	XGBoost	PCA	47.880	7.828
3	HR-NRI-VI	XGBoost	PCA	47.482	3.808
4	HR	XGBoost	No Filter	45.381	5.785
5	HR-NRI-VI	XGBoost	Borda	45.135	7.790
6	VI	XGBoost	No Filter	45.049	5.956
7	HR-NRI	XGBoost	PCA	44.683	7.252
8	NRI-VI	XGBoost	Pearson	44.507	7.410
9	VI	XGBoost	PCA	43.716	8.906
10	NRI-VI	XGBoost	Info Gain	42.859	6.678

Table 5: The overall best individual learner performance across any task and filter method for RF, SVM, XGBoost, Lasso and Ridge, sorted ascending by RMSE (p.p.) including the respective standard error (SE) of the cross-validation run. For extttregr.featureless the Task is no applicable and was therefore removed.

	Task	Model	Filter	RMSE	SE
1	HR	SVM	Relief	28.119	19.123
2	NRI	Lasso-MBO	No Filter	31.165	15.025
3	NRI	Ridge-MBO	No Filter	31.165	15.025
4	-	regr.featureless	No Filter	31.165	15.025
5	HR	RF	Relief	31.246	14.956
6	HR	XGBoost	Car	34.071	13.571

Table 6: Test fold performances in RMSE (p.p.) for learner SVM on the HR dataset without using a filter, showcasing performance variance on the fold level. For each row, the model was trained on observations from all others plots but the given one and tested on the observations of the given plot.

	RMSE	Test Plot
1	54.26	Laukiz1
2	28.12	Laukiz2
3	9.00	Luiando
4	21.17	Oiartzun

Table 7: Selected feature portions during tuning for the best performing learner-filter settings (SVM Relief, RF Relief, XGBoost CMIM) across folds for task HR-NRI-VI, sorted by plot name. 'Features (#)' denotes the absolute number of features selected and 'Features (%)' refers to the percentage relative to the overall features available in the training sets for each plot (Laukiz1 = 1249, Laukiz2 = 1357, Luiando = 1507, Oiartzun = 1311). Results were estimated in a separate model tuning step, not within the main cross-validation comparison.

Learner	Test Plot	Features (%)	Features (#)
RF Relief	Laukiz1	0.21573	3/1249
	Laukiz2	93.37086	1268/1357
	Luiando	99.97268	1507/1507
	Oiartzun	0.00405	1/1311
SVM Relief	Laukiz1	0.06200	1/1249
	Laukiz2	23.92820	325/1357
	Luiando	20.73514	313/1507
	Oiartzun	4.10636	54/1311
XGB CMIM	Laukiz1	98.12213	1226/1249
	Laukiz2	0.51526	7/1357
	Luiando	30.84900	465/1507
	Oiartzun	83.61298	1097/1311

### 3.3. Variable importance

#### 3.3.1. Permutation-based Variable Importance

The most important features for datasets HR and VI showed an average decrease in RMSE of 1.06 p.p. (HR, B69) and 1.93 p.p. (VI, Vogelmann2) (Figure 6). For dataset HR most features cluster around the infrared region (920 nm - 1000 nm) (six out of ten) while for VI eight out of ten concentrate on the wavelength range of 700 nm - 750 nm (the so called "red edge"). For feature set HR, four features in the infrared region (920 nm - 1000 nm) were identified by the model to be most important (causing a mean decrease

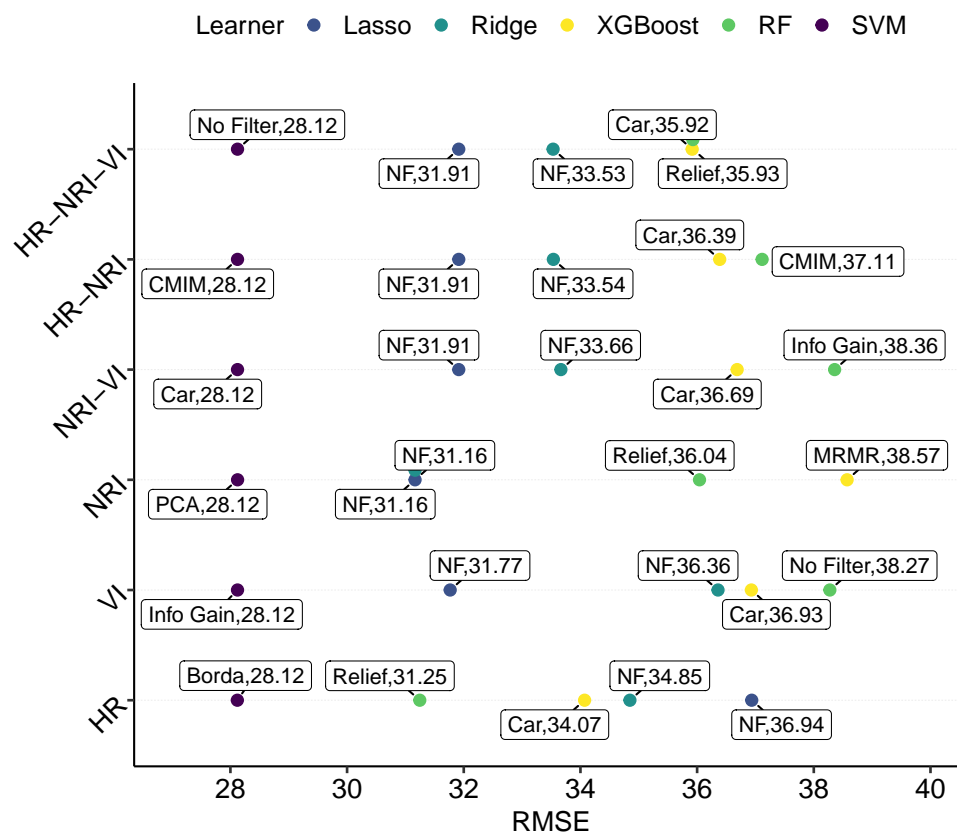


**Figure 3.** Predictive performance in RMSE (p.p.) of models across tasks. Different feature sets are shown on the y-axis. Labels show the feature selection method (e.g. NF = no filter, Car = 'Carscore', Info Gain = 'Information Gain', Borda = 'Borda').

in RMSE of around 1 p.p.). Overall, most features (excluding the top five respectively) showed only a small importance with average decreases in RMSE below 0.5 p.p..

## 4. Discussion

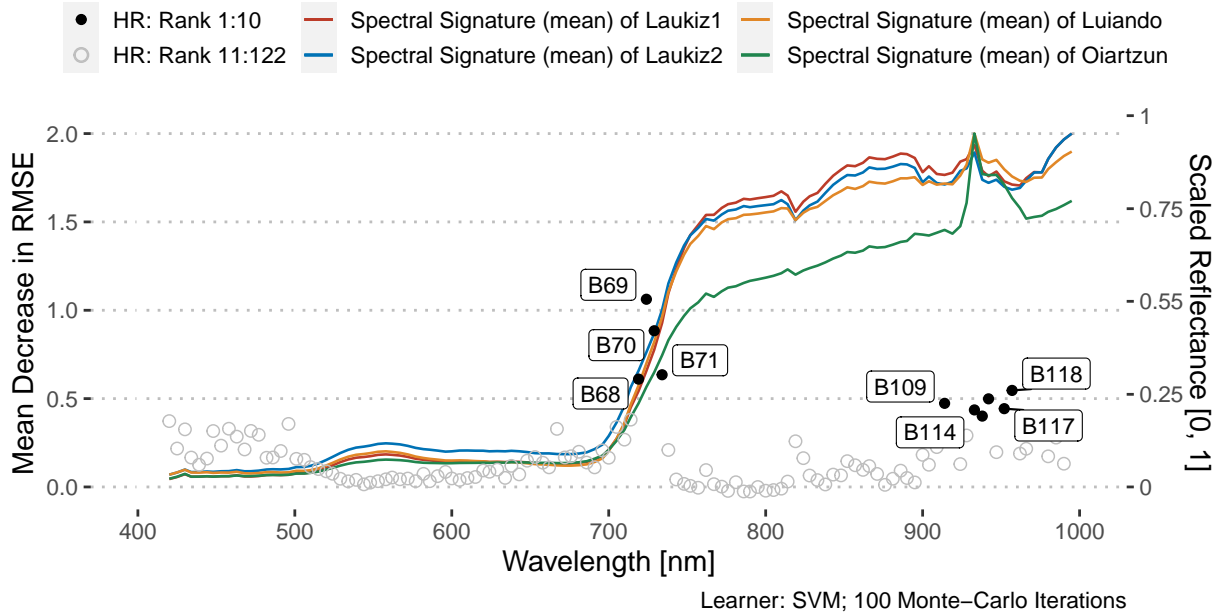
### 4.1. Predictive Performance

The best aggregated performance of this study (SVM + "Relief" filter, RMSE 28.12 p.p.) has to be seen in the light of model overfitting (see subsection 4.2). Leaving out the performance on Laukiz2 when aggregating results, the mean RMSE would be around 19 p.p. However, leaving out a single plot would also change the prediction results for the other plots because the observations from Laukiz2 would not be available for model training. Due to the apparent presence of model overfitting in this study it can be postulated that more training data representing a greater variety of situations is needed. A model can only make robust predictions if it has learned relationships across the whole range of the response. Hence, care should be taken when predicting to the landscape scale using models fitted on this dataset due to their lack of generalizability caused by the limitations of the available training data. However, when inspecting the fold level performances, it can be concluded that the models performed reasonably well predicting defoliation greater than 50% but failed for lower levels. This applied to all learners of this study. The overall performance of all learners achieved in this study can be classified as "poor" given that only the SVM learner was able to outperform the featureless learner (Table 5).

In addition, data quality issues (subsection 4.5) might have an influence on model performances. These include the timing of the acquisition of the hyperspectral data (late

### Permutation-based Variable Importance for dataset 'HR'

The ten most important features are labeled by their band number.



### Permutation-based Variable Importance for dataset 'VI'

The ten most important features are labeled by their index name.

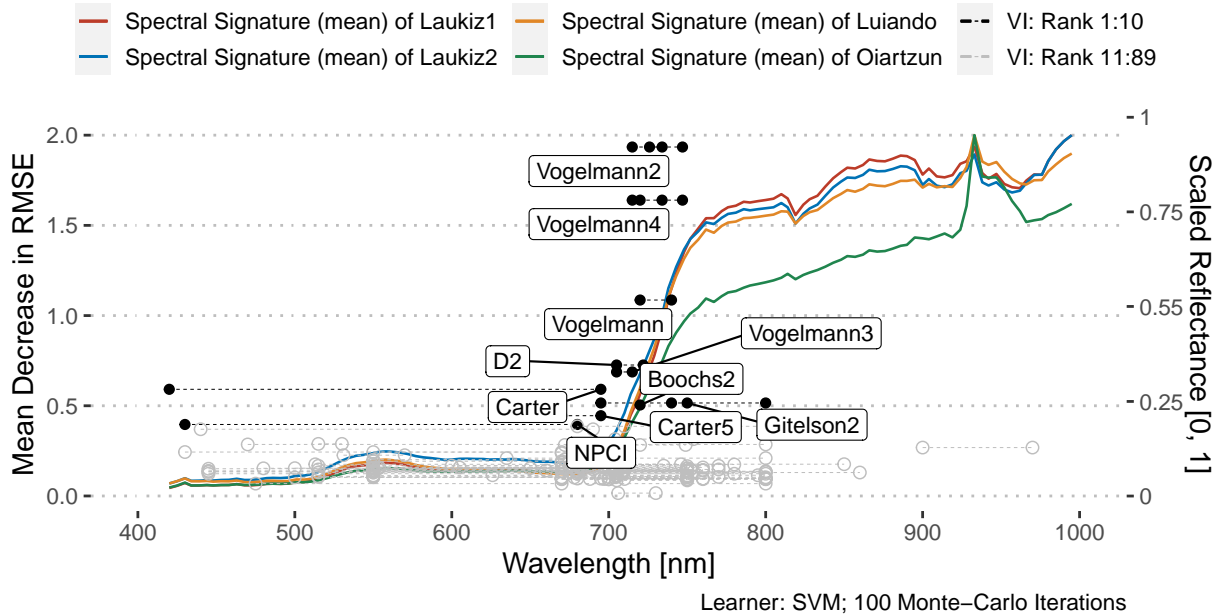


**Figure 6.** Variable importance for feature sets HR and VI: Mean decrease in RMSE for one-hundred feature permutations using the SVM learner. The wavelength range on the x-axis matches the range of the hyperspectral sensor (400 nm - 1000 nm). For each dataset, the ten most important features were highlighted as black dots and labeled by name. Grey dots represent features from importance rank 11 to last. The spectral signature (mean) of each plot was added as a reference on a normalized reflectance scale [0, 1] (secondary y-axis). VI features were decomposed into their individual formula parts; all instances being connected via dashed lines. Each VI feature is composed out of at least two instances.



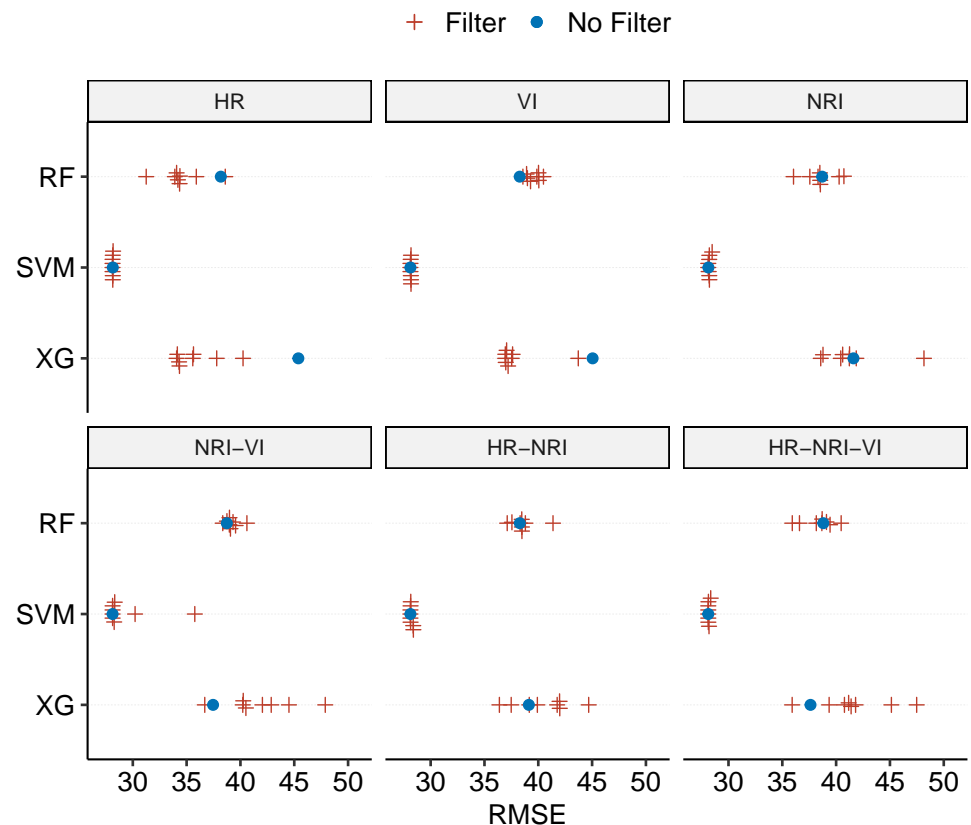


**Figure 4.** Model performances in RMSE across all tasks, split up in facets, when using no filter method (blue dot) compared to any other filter method (red cross) for learners RF, SVM and XGBoost (XG)

phenological phase), field measurement errors when surveying defoliation, the influence of background reflectance (e.g. soil reflectance) and the possible positional offset of measured GPS coordinates of trees.

#### 4.1.1. Model differences

An interesting finding is the strength of the SVM algorithm when comparing its predictive performance to its competitors (Table 5). These cluster around a performance of 31 p.p. while SVM is able to score about three p.p. better than all other methods. However, we refrain from comparing these results (both relatively and absolute) to other studies since many study design points have an influence on the final result (optimization strategy, data characteristics, feature selection methods, etc.).

A potential limiting factor in this study could be the upper limit of 70 iterations used for the XGBoost algorithm (hyperparameter rounds), especially for feature sets including NRIs (Table 8). This setting was a compromise between runtime and tuning space extension with the goal to work well for most feature sets. It may be recommendable to increase this upper limit to a value closer to the number of features in the dataset in order to be able to exploit the full potential of this hyperparameter.

#### 4.1.2. Feature set differences

One objective of this study was whether expert-based or data-driven feature engineering has a positive influence on model performance. With respect to Figure 3, no overall positive or negative trend was found for all models that related to specific feature sets. The performance of RF and XGBoost on the VI feature set was around four to six

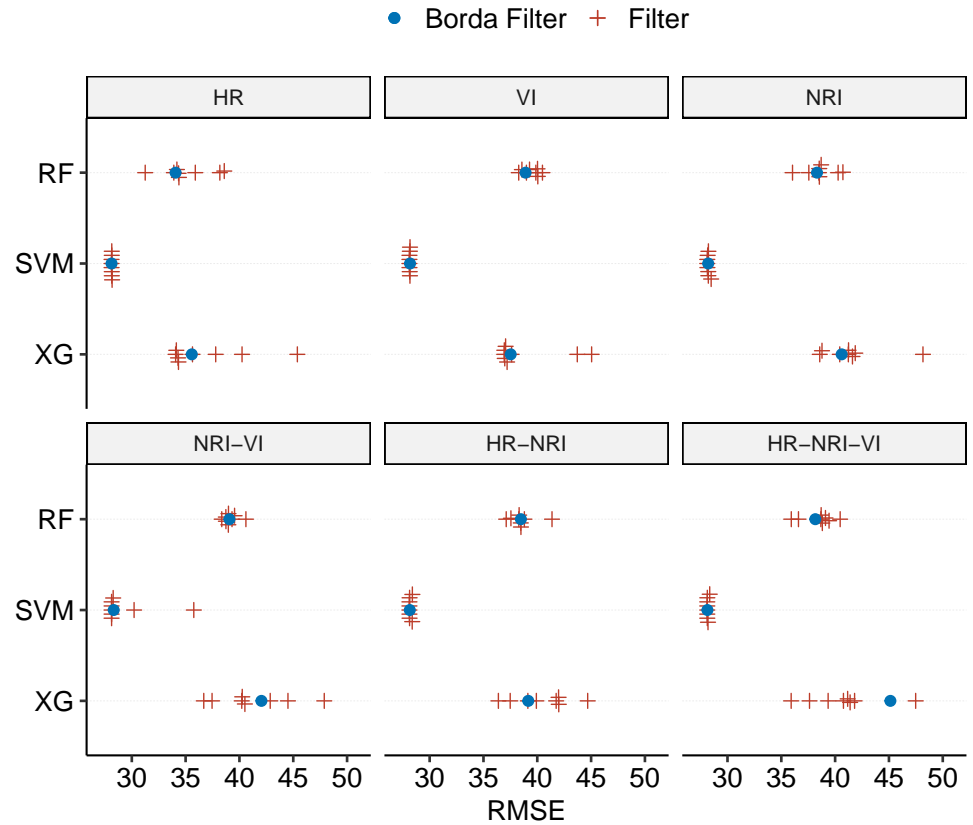


**Figure 5.** Predictive performances in RMSE (p.p.) when using the Borda filter method (blue dot) compared to any other filter (red cross) for each learner across all tasks.

417 p.p. lower than on others. One reason could be the lack of coverage in the wavelength  
 418 area between 810 nm and 1000 nm (Figure 6). In addition, for all learners but SVM a  
 419 better performance was observed when NRI indices were included in the feature set (i.e.  
 420 NRI-VI, HR-NRI, HR-NRI-VI).

#### 4.2. Performance vs. plot characteristics

422 The large differences in RMSE obtained on different test folds can be attributed  
 423 to model overfitting (Table 6). An RMSE of 54.26 p.p. reveals the model's inability to  
 424 predict tree defoliation on this plot (Laukiz2). Laukiz2 differs highly in the distribution of  
 425 the response variable defoliation compared to all other plots (Figure 1). In the prediction  
 426 scenario for Laukiz2, the model was trained on data containing mostly medium-to-high  
 427 defoliation values and only few low ones. This caused overfitting on the medium-to-high  
 428 values, degrading the model's predictive performance in other scenarios. When Laukiz2  
 429 was in the training set, the overall mean RMSE was reduced by up to 50% with single  
 430 fold performances as good as 9 p.p. RMSE (with Luiando as test set).

431 Arbitrary seeming values of selected feature percentages like 99.97268 % in Table 7  
 432 emerge from the specific setting which got elected as the best setting during the tuning  
 433 step. The specific value to benchmark during tuning is defined by the internal surrogate  
 434 learner of the MBO tuning method in this study and can be any numeric value between  
 435 0 and 1 (interpreted as percentage of available features).

436 Realizing early during hyperparameter optimization that only few features are  
 437 needed to reach adequate performances can reduce the overall computational runtime  
 438 substantially. Hence, regardless of the potential advantage of using filters for increased  
 439 predictive performance, these can have a strong positive effect on runtime, especially

on models which make use of hyperparameters that depend on the available number of features, such as RF  $m_{\text{try}}$ .

Ultimately, the results of Table 7 should be taken with care as they rely on single model-filter combinations and are subject to random variation. More in-depth research is needed to investigate the effect of filters on other criteria than performance (such as runtime), leading to a multi-criteria optimization problem.

#### 4.3. Feature selection methods

The usefulness of filters with respect to predictive performance in this study varied. While the performance of some models (up to five p.p. for RF and XGBoost) was improved by specific filters, some models achieved a poorer performance with filters than without them (Figure 4). No pattern with respect to lower scores related to a specific filter method could be found. Hence, it is recommended to test multiple filters in a study if filters are going to be used. While filters can improve the performance of models, they might be more interesting in other aspects than performance: reducing variables can reduce computational efforts in high-dimensional scenarios and might enhance the interpretability of models. Filters are a lot cheaper to compute than wrapper methods and the final feature subset selection can be integrated as an additional hyperparameter into the model optimization stage.

The models which used the Borda ensemble method in this study did not score better on average than models which used a single filter or no filter at all. Ensemble methods have higher stability and robustness than single ones and have shown promising results in [29]. Hence, their main advantage are stable performances across datasets with varying characteristics. Single filter methods might yield better model performances on certain datasets but fail on others. The fact that this study used multiple feature sets but only one dataset and tested many single filters could be a potential explanation why in all cases (besides RF on task HR-NRI-VI) a single filter outperformed the ensemble filter. However, studies which used ensemble filters are still rare and usually these are not compared against single filters [64]. In summary, Borda performs not better than a randomly selected filter method in this study. More case studies applying ensemble filter methods are needed to verify this finding. Nevertheless, ensemble filters can be a promising addition to a ML feature-selection portfolio.

PCA, acting as a filter method, more often showed less optimal results, especially for algorithms RF and XGBoost. Especially XGBoost had substantial problems when using PCA as a filter method and scored the worst four results (Table 4). However, PCA was able to reduce model fitting times substantially across all algorithms. Depending on the use case, PCA can be an interesting option to reduce dimensionality while keeping runtime low. However, information about the total number of features used by the model is lost when applying this technique. Since filter scores only need to be calculated once for a given dataset in a benchmark setting, the runtime advantage of a PCA vs. filter methods might in fact be negligible in practice.

#### 4.4. Linking feature importance to spectral characteristics

Not surprisingly the most important features for both HR and VI datasets were identified around the red edge of the spectra, specifically in the range of 680 nm to 750 nm.

This area has the highest ability to distinguish between reflectances related to a high density / high foliage density and thus the health status of vegetation and its respective counterpart [65]. However, four out of ten of the most important features of dataset HR are located between 920 nm and 1000 nm. Looking at the spectral curves of the plots, apparent reflectance differences can be observed in this spectral area - especially for plot Oiartzun - which might explain why these features were considered important by the model.

A possible explanation for the worse performances of most models scored on the VI dataset compared to all other feature sets could be the lack of features covering the area between 850 nm and 1000 nm (Figure 6). The majority of VI features covers the range between 550 nm - 800 nm. Only one index (PWI) covers information in the range beyond 900 nm.

#### 4.5. Data Quality

Environmental datasets always come with some constraints that can have potential influence on the modeling process and its outcome. Finding a suitable approach to extract the remote sensing information from each tree was a complex process. Due to the reported geometric offset of up to one meter within the hyperspectral data, the risk of assigning a value to an observation which would actually refer to a different, possibly non-tree, pixel was reasonably high. It was concluded that using a buffer of one meter can be a good compromise between the inclusion of information from too many surrounding trees, mapping a single tree crown accordingly accounting for a possible geometric offset. The applied buffer only included a pixel value if the distance to the centroid of a pixel was smaller than the buffer radius (i.e.  $\leq 1m$ ). This results in all cases in four contributing pixels (= four square meters) for the extraction of hyperspectral information for a given tree. Even though no results showing the influence of different buffer values on the extraction were provided, it is hypothesized that the relationships between features would not change substantially, leading to almost identical model results. Besides using a buffer to extract the hyperspectral information, a segmentation could have been considered. However, this method would have required more effort for no clear added value in our view and would have moved the focus of this manuscript more to data preprocessing and away from the focus on filter-based feature selection methods.

Another point worth discussing is that the exact number of contributing pixels to the final index value of an observation cannot be determined precisely: it depends on the location of the tree within the pixel grid. According to the extract function of the raster package, a pixel is included if its centroid (and not just any part of the grid cell) falls inside the buffer. As the buffer is circular, the total number of contributing pixels of each tree depends on the exact location of a tree within the pixel grid. If a tree observation is located on the border of the plot, some directions of the buffer will contain no values (because the image coverage was cropped to the borders of the plot) and the subsequent index value will be calculated with fewer pixels than if the tree observation is located in the middle of the plot. However, in most cases each tree information should be composed out of four hyperspectral pixels.

The available hyperspectral data covered a wavelength between 400 nm and 1000 nm. Hence, the wavelength range of the shortwave infrared (SWIR) region is not covered in this study. Given that this wavelength range is often used in forest health studies [66], e.g. when calculating the normalized difference moisture index (NDMI) index [67], this marks a clear limitation of the dataset at hand.

The dataset consists of in-situ data collected within September 2016 matched against remote sensing data acquired at the end of September 2016. A multi-temporal dataset consisting of in-situ data from different phenology stages would possibly improve the achieved model performances. However, this would also require matching hyperspectral data of these additional timestamps.

The R package *hsdar* was used for the calculation of vegetation indices [68]. All indices that could be calculated with the given spectral range of the data (400 nm - 1000 nm) were used. This means even though Table 9 lists all available indices of the package, not all listed indices were used in this study. Even though this selection included a large number of indices, some possibly helpful indices might have been missed due to the restriction of the hyperspectral data.

Overall, the magnitude of uncertainty introduced by the mentioned effects during index derivation cannot be quantified. Such limitations and uncertainties apply to most environmental studies and cannot be completely avoided.

#### 4.6. Comparison to other studies

While most defoliation studies operate on the plot level using coarser-resolution multispectral satellite data [10,69,70], there are also several recent studies using airborne or ground-based sensors at the tree level. Among these, [71,72] used ground-level methods such as airborne laser scanning (ALS) or light detection and ranging (LiDAR).

Studies focusing on tree-level defoliation mainly used ground-level methods such as ALS or LiDAR [71,72]. [71] used ordinary least squares (OLS) regression methods while [72] retrieved information from ground-level RGB photos using convolutional neural networks (CNN). However, both did not use spatial CV and [72] no feature selection (FS). [73] used a partial least-squares (PLS) model with high-resolution digital aerial photogrammetry (DAP) to predict cumulative defoliation caused by the spruce budworm. Study results indicated that spectral features were found to be most helpful for the model. Incorporating such (both spectral and structural) could be a possible enhancement for future works. No studies were found modeling defoliation caused by *Diplodia sapinea* (Fr.) Fuckel with remote sensing data and most studies focused on describing the tree conditions based on local sampling [74,75].

The field of (hyperspectral) remote sensing has a strong focus on using RF for modeling in recent years [76]. However, in high-dimensional scenarios, tuning parameter  $m_{try}$  becomes computationally expensive. To account for this and the high dimensionality in general, studies used feature selection approaches like semi-supervised feature extraction [77], wrapper methods [78–80], PCA and adjusted feature selection [81]. In general, applying feature selection methods on hyperspectral datasets has shown to be effective, regardless of the method used [82,83]. However, no study that made explicit use of filter methods in combination with hyperparameter tuning in the field of (hyperspectral) remote sensing could be found. Potential reasons for this absence could be an easier programmatic access to wrapper methods and a higher general awareness of such compared to filter methods. Applying the filter-based feature selection methodology shown in this study and its related code provided in the research compendium might be a helpful reference for future studies using hyperspectral remote sensing data.

When looking for remote sensing studies that compare multiple models, it turned out that these often operate in a low-dimensional predictor space [84] or use wrapper methods explicitly [80].

[85,86] are more similar in their methodology but focus on a different response variable (woody cover). [85] used machine learning with ALS data to study dieback of trees for eucalyptus forests. A grid search was used for hyperparameter tuning and forward feature selection (FFS) for variable selection. [86] analyzed woody cover in South Africa using spatial CV and FS approach [87] with a RF classifier. [88] shows a similar setup: they used hyperspectral vegetation indices, a nested CV approach for performance estimation and estimated variable importance targeting woody biomass as the response. In the results, lasso showed the best performance among the chosen methods. However, the authors did not optimize the hyperparameters of RF which makes a fair comparison problematic since the other models used perform internal optimization. The discussion section of [88] lists additional studies that made use of shrinkage models for high dimensional remote sensing modeling.

In summary, no studies which used filter methods for FS or made use of NRI indices in their work and had a relation to tree health could be found. This might relate to the fact that most environmental datasets are not high-dimensional. In fact, many studies use fewer than ten features and issues related to correlations are often solved manually instead of relying on an automated approach. This approach might suffer from subjectivity and may limit the reproducibility of results.



Other fields (e.g. bioinformatics) face high-dimensional datasets more often. Hence more studies using (filter-based) feature-selection approaches can be found for this field [89,90]. Yet bioinformatics differs conceptually in many ways from environmental modeling and therefore no greater focus was put into comparing studies of this field. The availability of high dimensional feature sets will increase in the future due to higher temporal and spectral resolutions of sensors. In addition, a high spatial resolution comes with the possibility to calculate many textural features. Hence, the ability to deal with high dimensional datasets becomes more important and unbiased robust approaches are needed. We hope that this work and its methodology raises awareness about the application of filter methods to tackle high-dimensional problems in the environmental modeling field.

## 5. Conclusions

This study analyzed defoliation of trees in northern Spain by using hyperspectral data as input for ML models which used hyperparameter tuning and filter-based feature selection. Substantial differences in performance occurred depending on which feature selection and machine learning methods were combined. SVM showed the most robust behavior across all highly-correlated datasets and was able to predict the response variable of this study substantially better than other methods.

Filter methods were able to improve the predictive performance on datasets in some instances, although there was no clear and systematic pattern. Their effectiveness depends on the algorithm and the dataset characteristics. Ensemble filter methods did not show a substantial improvement over individual filter methods in this study.

The addition of derived feature sets was in most cases able to improve predictive performance. In contrast, feature sets which focused on only a small fraction of the available spectral range (i.e. dataset VI) showed a worse performance than the ones which covered wider range (400 nm - 1000 nm; HR, NRI). NRIs can be seen as a valuable addition for optimizing predictive performance in remote sensing of vegetation.

Features along the red edge wavelength region were most important for models during prediction. With respect to dedicated vegetation indices, all versions of the Vogelmann index were seen as the most important index for the best performing SVM model. This matches well with the actual purpose of these indices: These were invented to detect defoliation on sugar maple trees (*Acer saccharum* Marsh.) caused by pear thrips (*Taeniothrips inconsequens* Uzel) [91]. However, assessing the feature importance for highly correlated features remains a challenging task. Results might be biased and should be taken with care to avoid overgeneralizing from individual studies.

Finally, the potential of predicting defoliation with the given study design was rather limited with respect to the average RMSE of 28 p.p. scored by the best performing model. More training data covering a wider range of defoliation values in a larger number of forest plantations is needed to train better models which can create more robust predictions.

**Author Contributions:** Conceptualization, Patrick Schratz and Alexander Brenning; Data curation, Patrick Schratz and Eugenia Iturritxa; Formal analysis, Patrick Schratz, José Cortés, Bernd Bischl and Alexander Brenning; Funding acquisition, Alexander Brenning; Investigation, Patrick Schratz; Methodology, Patrick Schratz, Jannes Münchow, José Cortés and Bernd Bischl; Project administration, Alexander Brenning; Resources, Eugenia Iturritxa; Software, Patrick Schratz; Supervision, Bernd Bischl and Alexander Brenning; Validation, Patrick Schratz and Alexander Brenning; Visualization, Patrick Schratz; Writing – original draft, Patrick Schratz; Writing – review & editing, Jannes Münchow, José Cortés and Alexander Brenning.

**Funding:** This work was funded by the EU LIFE Healthy Forest project (LIFE14 ENV/ES/000179) and the German Scholars Organization/Carl Zeiss Foundation.

**Data Availability Statement:** The data presented in this study are openly available in Zenodo at <https://doi.org/10.5281/zenodo.2635403>.

**Conflicts of Interest:** The authors declare no conflict of interest. The funders had no role in the design of the study; in the collection, analyses, or interpretation of data; in the writing of the manuscript, or in the decision to publish the results.

## Abbreviations

The following abbreviations are used in this manuscript:

AGB	above-ground biomass
ALE	accumulated local effects
ALS	airborne laser scanning
ANN	artificial neural network
AUROC	area under the receiver operating characteristics curve
BRT	boosted regression trees
CART	classification and regression trees
CNN	convolutional neural networks
CV	cross-validation
DAP	digital aerial photogrammetry
ENM	environmental niche modeling
FFS	forward feature selection
FPR	false positive rate
FS	feature selection
GAM	generalized additive model
GBM	gradient boosting machine
GLM	generalized linear model
ICGC	Institut Cartografic i Geologic de Catalunya
IQR	interquartile range
LiDAR	light detection and ranging
LOWESS	locally weighted scatter plot smoothing
MARS	multivariate adaptive regression splines
MBO	model-based optimization
MEM	maximum entropy model
ML	machine learning
NDII	normalized difference infrared index
NDMI	normalized difference moisture index
NIR	near-infrared
NRI	normalized ratio index
OLS	ordinary least squares
OMNBR	optimized multiple narrow-band reflectance
PCA	principal component analysis
PDP	partial dependence plots
PISR	potential incoming solar radiation
PLS	partial least-squares
POV	proportion of variance explained
RBF	radial basis function
RF	random forest
RMSE	root mean square error
RR	ridge regression
RSS	residual sum of squares
SAR	synthetic aperture radar
SDM	species distribution modeling
SMBO	sequential-based model optimization
SVM	support vector machine
TPR	true positive rate
VI	vegetation index
XGBoost	extreme gradient boosting

## 653 Appendix A Appendices

### 654 Appendix A.1

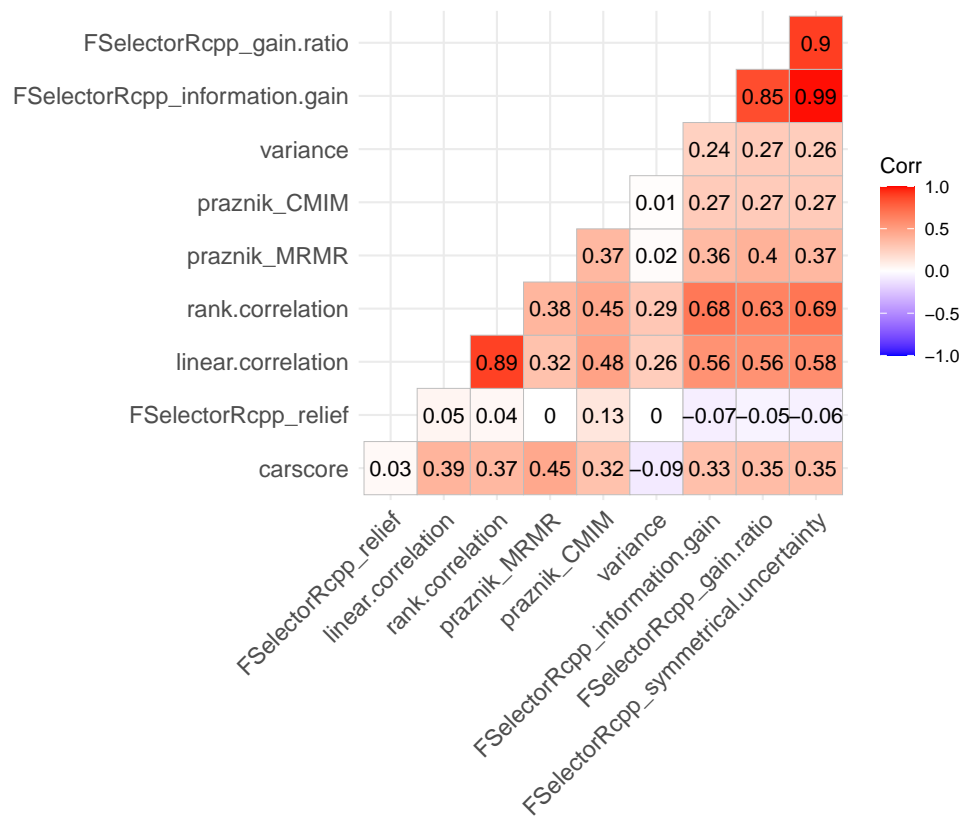


**Figure A1.** Spearman correlations of NRI feature rankings obtained with different filters. Filter names refer to the nomenclature used by the mlr R package. Underscores in names divide the terminology into their upstream R package and the actual filter name.

655 *Appendix A.2*

Table 8: Hyperparameter ranges and types for each model. Hyperparameter notations from the respective R packages are shown.

Model (package)	Hyperparameter	Type	Start	End	Default
RF (ranger)	$x_{try}$	dbl	0	0.5	-
	min.node.size	int	1	10	1
	sample.fraction	dbl	0.2	0.9	1
SVM (kernlab)	C	dbl	$2^{-10}$	$2^{10}$	1
	$\sigma$	dbl	$2^{-5}$	$2^5$	1
XGBoost (xgboost)	nrounds	int	10	70	-
	colsample_bytree	dbl	0.6	1	1
	subsample	dbl	0.6	1	1
	max_depth	int	3	15	6
	gamma	int	0.05	10	0
	eta	dbl	0.1	1	0.3
	min_child_weight	int	1	7	1

656 *Appendix A.3*Table 9: List of available vegetation indices in the *hsdar* package.

Name	Formula	Reference*
Boochs	$D_{703}$	[92]
Boochs2	$D_{720}$	[92]
CAI	$0.5 \times (R_{2000} + R_{2200}) - R_{2100}$	[93]
CARI	$a = (R_{700} - R_{550}) / 150$ $b = R_{550} - (a \times 550)$ $\frac{R_{700} \times  (a \times 670 + R_{670} + b) }{R_{670} \times (a^2 + 1)^{0.5}}$	[94]
Carter	$R_{695} / R_{420}$	[95]
Carter2	$R_{695} / R_{760}$	[95]
Carter3	$R_{605} / R_{760}$	[95]
Carter4	$R_{710} / R_{760}$	[95]
Carter5	$R_{695} / R_{670}$	[95]
Carter6	$R_{550}$	[95]
CI	$R_{675} \times R_{690} / R_{683}^2$	[96]
657 CI2	$R_{760} / R_{700} - 1$	[97]
CIInt	$\int_{600nm}^{735nm} R$	[98]
CRI1	$1 / R_{515} - 1 / R_{550}$	[97]
CRI2	$1 / R_{515} - 1 / R_{770}$	[97]
CRI3	$1 / R_{515} - 1 / R_{550} \times R_{770}$	[97]
CRI4	$1 / R_{515} - 1 / R_{700} \times R_{770}$	[97]
D1	$D_{730} / D_{706}$	[96]
D2	$D_{705} / D_{722}$	[96]
Datt	$(R_{850} - R_{710}) / (R_{850} - R_{680})$	[99]
Datt2	$R_{850} / R_{710}$	[99]
Datt3	$D_{754} / D_{704}$	[99]
Datt4	$R_{672} / (R_{550} \times R_{708})$	[100]
Datt5	$R_{672} / R_{550}$	[100]
Datt6	$(R_{860}) / (R_{550} \times R_{708})$	[100]
Datt7	$(R_{860} - R_{2218}) / (R_{860} - R_{1928})$	[101]



	Datt8	$(R_{860} - R_{1788}) / (R_{860} - R_{1928})$	[101]
	DD	$(R_{749} - R_{720}) - (R_{701} - R_{672})$	[102]
	DDn	$2 \times (R_{710} - R_{660} - R_{760})$	[103]
	DPI	$(D_{688} * D_{710}) / D_{697}^2$	[96]
	DWSI1	$R_{80} / R_{1660}$	[104]
	DWSI2	$R_{1660} / R_{550}$	[104]
	DWSI3	$R_{1660} / R_{680}$	[104]
	DWSI4	$R_{550} / R_{680}$	[104]
	DWSI5	$(R_{800} + R_{550}) / (R_{1660} + R_{680})$	[104]
	EGFN	$\frac{(\max(D_{650:750}) - \max(D_{500:550}))}{(\max(D_{650:750}) + \max(D_{500:550}))}$	[105]
	EGFR	$\max(D_{650:750}) / \max(D_{500:550})$	[105]
	EVI	$\frac{2.5 \times ((R_{800} - R_{670}))}{(R_{800} - (6 \times R_{670}) - (7.5 \times R_{475}) + 1)}$	[106]
	GDVI	$(R_{800}^n - R_{680}^n) / (R_{800}^n + R_{680}^n)^{**}$	[107]
	GI	$R_{554} / R_{677}$	[108]
	Gitelson	$1 / R_{700}$	[109]
658	Gitelson2	$(R_{750} - R_{800} / R_{695} - R_{740}) - 1$	[97]
	GMI1	$R_{750} / R_{550}$	[97]
	GMI2	$R_{750} / R_{700}$	[97]
	Green NDVI	$\frac{R_{800} - R_{550}}{R_{800} + R_{550}}$	[110]
	LWVI_1	$\frac{(R_{1094} - R_{983})}{(R_{1094} + R_{983})}$	[111]
	LWVI_2	$\frac{R_{1094} - R_{1205}}{R_{1094} + R_{1205}}$	[111]
	Maccioni	$\frac{R_{780} - R_{710}}{R_{780} - R_{680}}$	[112]
	MCARI	$((R_{700} - R_{670}) - 0.2 \times (R_{700} - R_{550})) \times (R_{700} / R_{670})$	[113]
	MCARI2	$((R_{750} - R_{705}) - 0.2 \times (R_{750} - R_{550})) \times (R_{750} / R_{705})$	[114]
	mND705	$\frac{(R_{750} - R_{705})}{R_{750} + R_{705} - 2 \times R_{445}}$	[115]
	mNDVI	$\frac{(R_{800} - R_{680})}{R_{800} + R_{680} - 2 \times R_{445}}$	[115]
	MPRI	$\frac{R_{515} - R_{530}}{R_{515} + R_{530}}$	[116]
	MSAVI	$0.5 \times ((2 \times R_{800} + 1)^2 - 8 \times (R_{800} - R_{670}))^{0.5}$	[117]
	MSI	$\frac{R_{1600}}{R_{817}}$	[118]
	mSR	$\frac{R_{800} - R_{445}}{R_{680} - R_{445}}$	[115]

mSR2	$\frac{(R_{750}/R_{705})-1}{R_{750}/R_{705}+1)^{0.5}}$	[119]
mSR705	$\frac{R_{750}-R_{445}}{R_{705}-R_{445}}$	[115]
MTCI	$\frac{R_{754}-R_{709}}{R_{709}-R_{681}}$	[120]
MTVI	$1.2 \times (1.2 \times (R_{800} - R_{550}) - 2.5 \times (R_{670} - R_{550}))$	[121]
NDLI	$\frac{\log(1/R_{1754})-\log(1/R_{1680})}{\log(1/R_{1754})+\log(1/R_{1680})}$	[122]
NDNI	$\frac{\log(1/R_{1510})-\log(1/R_{1680})}{\log(1/R_{1510})+\log(1/R_{1680})}$	[122]
NDVI	$\frac{R_{800}-R_{680}}{R_{800}+R_{680}}$	[123]
NDVI2	$\frac{R_{750}-R_{705}}{R_{750}+R_{705}}$	[124]
NDVI3	$\frac{R_{682}-R_{553}}{R_{682}+R_{553}}$	[125]
NDWI	$\frac{R_{860}-R_{1240}}{R_{860}+R_{1240}}$	[67]
NPCI	$\frac{R_{680}-R_{430}}{R_{680}+R_{430}}$	[105]
OSAVI	$\frac{(1+0.16) \times (R_{800}-R_{670})}{R_{800}+R_{670}+0.16}$	[126]
OSAVI2	$\frac{(1+0.16) \times (R_{750}-R_{705})}{R_{750}+R_{705}+0.16}$	[114]
PARS	$\frac{R_{746}}{R_{513}}$	[127]
PRI	$\frac{R_{531}-R_{570}}{R_{531}+R_{570}}$	[128]
PRI_norm	$\frac{PRI \times (-1)}{RDVI \times R_{700}/R_{670}}$	[129]
PRI*CI2	$PRI * CI2$	[130]
PSRI	$\frac{R_{678}-R_{500}}{R_{750}}$	[131]
PSSR	$\frac{R_{800}}{R_{635}}$	[132]
PSND	$\frac{R_{800}-R_{470}}{R_{800}-R_{470}}$	[132]
PWI	$\frac{R_{900}}{R_{970}}$	[133]
RDVI	$\frac{R_{800}-R_{670}}{\sqrt{R_{800}+R_{670}}}$	[134]
REP_LE	Red-edge position through linear extrapolation	[135]
REP_Li	$R_{re} = \frac{R_{670}+R_{780}}{2}$ $\frac{700+40 \times ((R_{re}-R_{700})}{(R_{740}-R_{700}))}$	[136]
SAVI	$\frac{(1+L) \times (R_{800}-R_{670})}{(R_{800}+R_{670}+L)}$	[137]
SIPI	$\frac{R_{800}-R_{445}}{R_{800}-R_{680}}$	[138]
SPVI	$0.4 \times 3.7 \times (R_{800} - R_{670}) - 1.2 \times ((R_{530} - R_{670})^2)^{0.5}$	[139]
SR	$\frac{R_{800}}{R_{680}}$	[140]
SR1	$\frac{R_{750}}{R_{700}}$	[141]

SR2	$\frac{R_{752}}{R_{690}}$	[141]
SR3	$\frac{R_{750}}{R_{550}}$	[141]
SR4	$\frac{R_{700}}{R_{670}}$	[142]
SR5	$\frac{R_{675}}{R_{700}}$	[127]
SR6	$\frac{R_{750}}{R_{710}}$	[143]
SR7	$\frac{R_{440}}{R_{690}}$	[144]
SR8	$\frac{R_{515}}{R_{550}}$	[145]
SRPI	$\frac{R_{430}}{R_{680}}$	[138]
SRWI	$\frac{R_{850}}{R_{1240}}$	[96]
Sum_Dr1	$\sum_{i=626}^{795} D1_i$	[146]
Sum_Dr2	$\sum_{i=680}^{780} D1_i$	[147]
SWIR FI	$\frac{R_{2133}^2}{R_{2225} \times R_{2209}^3}$	[148]
SWIR LI	$3.87 \times (R_{2210} - R_{2090}) - 27.51 \times (R_{2280} - R_{2090}) - 0.2$	[149]
SWIR SI	$-41.59 \times (R_{2210} - R_{2090}) + 1.24 \times (R_{2280} - R_{2090}) + 0.64$	[149]
SWIR VI	$37.72 \times (R_{2210} - R_{2090}) + 6.27 \times (R_{2280} - R_{2090}) + 0.57$	[149]
TCARI	$3 * ((R_{700} - R_{670}) - 0.2 \times R_{700} - R_{550}) \times (R_{700} / R_{670})$	[121]
TCARI/OSAVI	TCARI/OSAVI	[121]
TCARI2	$3 \times ((R_{750} - R_{705}) - 0.2 \times (R_{750} - R_{550}) \times (R_{750} / R_{705}))$	[114]
TCARI2/OSAVI2	TCARI2/OSAVI2	[114]
TGI	$-0.5(190(R_{670} - R_{550}) - 120(R_{670} - R_{480}))$	[150]
TVI	$0.5 \times (120 \times (R_{750} - R_{550}) - 200 \times (R_{670} - R_{550}))$	[151]
Vogelmann	$\frac{R_{740}}{R_{720}}$	[91]
Vogelmann2	$\frac{R_{734} - R_{747}}{R_{715} + R_{726}}$	[91]
Vogelmann3	$\frac{D_{715}}{D_{705}}$	[91]
Vogelmann4	$\frac{R_{734} - R_{747}}{R_{715} + R_{720}}$	[91]

#### 661 Appendix A.4

662 The following information was provided by the Institut Carogràfic i Geològic de  
663 Catalunya, which was in charge of image acquisition and data preprocessing.

664 The AISA EAGLE-II sensor was used for airborne image acquisition with a field of  
665 view of 37.7°. Its spectral resolution is 2.4 nm and ranged from 400 to 1000 nm.

666 The conversion of Digital Numbers (DN) to spectral radiance was made by using a  
667 software designed for the instrument. Images were originally scaled in 12 bits but were  
668 radiometrically calibrated to 16 bits, reserving the highest value (65535) for null values.  
669 The procedure was applied to the 23 previously selected images. Last, the geometric and  
670 atmospheric corrections were applied to the images.

671 The aim of this procedure was to reduce the positional errors of the images. The  
672 cartographic reference system in use was EPSG 25830. Positioning was done by coupling  
673 an Applanix POS AV 410 system to the sensor, integrating GPS and IMU systems. The  
674 system provides geographic coordinates of the terrain and relative coordinates of the  
675 aircraft (attitude) at each scanned line. Additionally a DSM from GeoEuskadi with a  
676 spatial resolution of 1 m was used. The orthorectified hyperspectral images were compared  
677 to orthoimages (1:5000) from GeoEuskadi. This comparison was used as the base to  
678 calculate RMSE, which was below the ground sampling distance in the across and along  
679 track directions.

680 The radiance measured by an instrument depends on the illumination geometry and  
681 the reflective properties of the observed surface. Radiation may be absorbed or scattered  
682 (Rayleigh and Mie scattering). Scattering is responsible for the adjacency effect, i.e.,  
683 radiation coming from neighbors areas to the target pixel. The MODTRAN algorithm was  
684 used to model the effect of the atmosphere on the radiation. To represent the aerosols of  
685 the study area, the rural model was used. In addition the optical thickness was estimated  
686 on pixels with a high vegetation cover. Columnar water vapor was estimated by a linear  
687 regression ratio where the spectral radiance of each pixel at the band of the maximum  
688 water absorption (906 nm) is compared to its theoretical value in absence of absorption.  
689 Nonetheless, this technique is unreliable in presence of a spectral resolution as in this  
690 case. To resolve this, the water vapor parameter was selected manually according to the  
691 smoothness observed on the reflectance peak at 960 nm. This was combined with an  
692 mid-latitude summer atmosphere model. The output of this procedure was reflectance  
693 from the target pixel scaled between 0 and 10,000.

694 The image acquisitions were originally attempted during one day (29.10.2016). Due  
695 to the variable meteorological conditions some stands had to be imaged one day later.

## References

1. Lary, D.J.; Alavi, A.H.; Gandomi, A.H.; Walker, A.L. Machine learning in geosciences and remote sensing. *Geoscience Frontiers* **2016**, *7*, 3–10. doi:10.1016/j.gsf.2015.07.003.
2. Ma, Y.; Wu, H.; Wang, L.; Huang, B.; Ranjan, R.; Zomaya, A.; Jie, W. Remote sensing big data computing: Challenges and opportunities. *Future Generation Computer Systems* **2015**, *51*, 47–60. doi:10/gdq98h.
3. Mascaro, J.; Asner, G.P.; Knapp, D.E.; Kennedy-Bowdoin, T.; Martin, R.E.; Anderson, C.; Higgins, M.; Chadwick, K.D. A Tale of Two “Forests”: Random Forest Machine Learning Aids Tropical Forest Carbon Mapping. *PLOS ONE* **2014**, *9*, e85993. doi:10/f5vmrb.
4. Urban, M.; Berger, C.; Mudau, T.E.; Heckel, K.; Truckenbrodt, J.; Onyango Odipo, V.; Smit, I.P.J.; Schullius, C. Surface Moisture and Vegetation Cover Analysis for Drought Monitoring in the Southern Kruger National Park Using Sentinel-1, Sentinel-2, and Landsat-8. *Remote Sensing* **2018**, *10*, 1482. doi:10/gf3xhw.
5. Hawryło, P.; Bednarsz, B.; Wezyk, P.; Szostak, M. Estimating defoliation of Scots pine stands using machine learning methods and vegetation indices of Sentinel-2. *European Journal of Remote Sensing* **2018**, *51*, 194–204. doi:10/gf3rbq.
6. Pollastrini, M.; Feducci, M.; Bonal, D.; Fotelli, M.; Gessler, A.; Grossiord, C.; Guyot, V.; Jactel, H.; Nguyen, D.; Radoglou, K.; Bussotti, F. Physiological significance of forest tree defoliation: Results from a survey in a mixed forest in Tuscany (central Italy). *Forest Ecology and Management* **2016**, *361*, 170–178. doi:10.1016/j.foreco.2015.11.018.
7. Gottardini, E.; Cristofolini, F.; Cristofori, A.; Pollastrini, M.; Camin, F.; Ferretti, M. A multi-proxy approach reveals common and species-specific features associated with tree defoliation in broadleaved species. *Forest Ecology and Management* **2020**, *467*, 118151. doi:10.1016/j.foreco.2020.118151.

8. Oliva, J.; Stenlid, J.; Grönkvist-Wichmann, L.; Wahlström, K.; Jonsson, M.; Drobyshev, I.; Stenström, E. Pathogen-induced defoliation of *Pinus sylvestris* leads to tree decline and death from secondary biotic factors. *Forest Ecology and Management* **2016**, *379*, 273–280. doi:10.1016/j.foreco.2016.08.011.
9. Zhang, K.; Thapa, B.; Ross, M.; Gann, D. Remote sensing of seasonal changes and disturbances in mangrove forest: a case study from South Florida. *Ecosphere* **2016**, p. e01366. doi:10.1002/ecs2.1366@10.1002/(ISSN)2150-8925.ExtremeColdSpells.
10. Townsend, P.A.; Singh, A.; Foster, J.R.; Rehberg, N.J.; Kingdon, C.C.; Eshleman, K.N.; Seagle, S.W. A general Landsat model to predict canopy defoliation in broadleaf deciduous forests. *Remote Sensing of Environment* **2012**, *119*, 255–265. doi:10.1016/j.rse.2011.12.023.
11. Jiang, Y.; Wang, T.; de Bie, C.A.J.M.; Skidmore, A.K.; Liu, X.; Song, S.; Zhang, L.; Wang, J.; Shao, X. Satellite-derived vegetation indices contribute significantly to the prediction of epiphyllous liverworts. *Ecological Indicators* **2014**, *38*, 72–80. doi:10.1016/j.ecolind.2013.10.024.
12. Adamczyk, J.; Osberger, A. Red-edge vegetation indices for detecting and assessing disturbances in Norway spruce dominated mountain forests. *International Journal of Applied Earth Observation and Geoinformation* **2015**, *37*, 90–99. doi:10.1016/j.jag.2014.10.013.
13. Thenkabail, P.S.; Lyon, J.G.; Huete, A., Eds. *Hyperspectral indices and image classifications for agriculture and vegetation*; CRC Press, 2018. doi:10.1201/9781315159331.
14. Thenkabail, P.S.; Smith, R.B.; De Pauw, E. Hyperspectral vegetation indices and their relationships with agricultural crop characteristics. *Remote sensing of Environment* **2000**, *71*, 158–182.
15. Cai, J.; Luo, J.; Wang, S.; Yang, S. Feature selection in machine learning: A new perspective. *Neurocomputing* **2018**, *300*, 70–79. doi:10.1016/j.neucom.2017.11.077.
16. Trunk, G.V. A Problem of Dimensionality: A Simple Example. *IEEE Transactions on Pattern Analysis and Machine Intelligence* **1979**, *PAMI-1*, 306–307. doi:10/bb2j4t.
17. Xu, H.; Caramanis, C.; Mannor, S. Statistical Optimization in High Dimensions. *Operations Research* **2016**, *64*, 958–979. doi:10/f8zbmj.
18. Mesanza, N.; Iturritxa, E.; Patten, C.L. Native rhizobacteria as biocontrol agents of *Heterobasidion annosum* s.s. and *Armillaria mellea* infection of *Pinus radiata*. *Biological Control* **2016**, *101*, 8–16. doi:10.1016/j.biocontrol.2016.06.003.
19. Iturritxa, E.; Trask, T.; Mesanza, N.; Raposo, R.; Elvira-Recuenco, M.; Patten, C.L. Biocontrol of *Fusarium circinatum* infection of young *Pinus radiata* trees. *Forests* **2017**, *8*, 32. doi:10.3390/f8020032.
20. Iturritxa, E.; Mesanza, N.; Brenning, A. Spatial analysis of the risk of major forest diseases in Monterey pine plantations. *Plant Pathology* **2014**, *64*, 880–889. doi:10.1111/ppa.12328.
21. Ganley, R.J.; Watt, M.S.; Manning, L.; Iturritxa, E. A global climatic risk assessment of pitch canker disease. *Canadian Journal of Forest Research* **2009**, *39*, 2246–2256. doi:10.1139/x09-131.
22. Innes, J. Methods to estimate forest health. *Silva Fennica* **1993**, *27*. doi:10.14214/sf.a15668.
23. MacLean, D.A.; Lidstone, R.G. Defoliation by spruce budworm: estimation by ocular and shoot-count methods and variability among branches, trees, and stands. *Canadian Journal of Forest Research* **1982**, *12*, 582–594. doi:10.1139/x82-090.
24. Johnstone Iain M.; Titterton D. Michael. Statistical challenges of high-dimensional data. *Philosophical Transactions of the Royal Society A: Mathematical, Physical and Engineering Sciences* **2009**, *367*, 4237–4253. doi:10/cbk4qk.
25. Bommert, A.; Sun, X.; Bischl, B.; Rahnenführer, J.; Lang, M. Benchmark for filter methods for feature selection in high-dimensional classification data. *Computational Statistics & Data Analysis* **2020**, *143*, 106839. doi:10.1016/j.csda.2019.106839.
26. Das, S. Filters, Wrappers and a Boosting-Based Hybrid for Feature Selection. ICML, 2001.
27. Guyon, I.; Elisseeff, A. An introduction to variable and feature selection. *Journal of Machine Learning Research* **2003**, *3*, 1157–1182.
28. Jolliffe, I.; Cadima, J. Principal component analysis: a review and recent developments. *Philosophical Transactions of the Royal Society A: Mathematical, Physical and Engineering Sciences* **2016**, *374*, 20150202. doi:10/gcsfk7.
29. Drotár, P.; Šimoňák, S.; Pietriková, E.; Chovanec, M.; Chovancová, E.; Ádám, N.; Szabó, C.; Baláz, A.; Biñas, M. Comparison of Filter Techniques for Two-Step Feature Selection. *Computing and Informatics* **2017**, *36*, 597–617. doi:10.4149/cai\_2017\_3\_597.
30. Drotár, P.; Gazda, J.; Smékal, Z. An experimental comparison of feature selection methods on two-class biomedical datasets. *Computers in Biology and Medicine* **2015**, *66*, 1–10. doi:10.1016/j.combiomed.2015.08.010.
31. Abeel, T.; Helleputte, T.; Van de Peer, Y.; Dupont, P.; Saeys, Y. Robust biomarker identification for cancer diagnosis with ensemble feature selection methods. *Bioinformatics* **2010**, *26*, 392–398. doi:10/dfznxv.
32. Dietterich, T.G. Ensemble Methods in Machine Learning. Proceedings of the First International Workshop on Multiple Classifier Systems. Springer-Verlag, 2000, pp. 1–15.
33. Polikar, R. Ensemble Learning. In *Ensemble Machine Learning: Methods and Applications*; Zhang, C.; Ma, Y., Eds.; Springer US: Boston, MA, 2012; pp. 1–34. doi:10.1007/978-1-4419-9326-7\_1.
34. Feurer, M.; Klein, A.; Eggensperger, K.; Springenberg, J.; Blum, M.; Hutter, F. Efficient and Robust Automated Machine Learning. In *Advances in Neural Information Processing Systems 28*; Cortes, C.; Lawrence, N.D.; Lee, D.D.; Sugiyama, M.; Garnett, R., Eds.; Curran Associates, Inc., 2015; pp. 2962–2970.
35. Bolón-Canedo, V.; Alonso-Betanzos, A. Ensembles for feature selection: A review and future trends. *Information Fusion* **2019**, *52*, 1–12. doi:10.1016/j.inffus.2018.11.008.



36. Pearson, K. LIII. On lines and planes of closest fit to systems of points in space. *The London, Edinburgh, and Dublin Philosophical Magazine and Journal of Science* **1901**, *2*, 559–572. doi:10/dd63n4.
37. Quinlan, J.R. Induction of decision trees. *Machine Learning* **1986**, *1*, 81–106. doi:10/ctd6mv.
38. Zhao, X.M. Maximum Relevance/Minimum Redundancy (MRMR). In *Encyclopedia of Systems Biology*; Dubitzky, W.; Wolkenhauer, O.; Cho, K.H.; Yokota, H., Eds.; Springer New York: New York, NY, 2013; pp. 1191–1192. doi:10.1007/978-1-4419-9863-7\_432.
39. Zuber, V.; Strimmer, K. High-Dimensional Regression and Variable Selection Using CAR Scores. *Statistical Applications in Genetics and Molecular Biology* **2011**, *10*. doi:10/c62xhp.
40. Kira, K.; Rendell, L.A. The feature selection problem: traditional methods and a new algorithm. Proceedings of the tenth national conference on Artificial intelligence. AAAI Press, 1992, pp. 129–134.
41. Fleuret, F. Fast Binary Feature Selection with Conditional Mutual Information. *The Journal of Machine Learning Research* **2004**, *5*, 1531–1555.
42. Shannon, C.E. A mathematical theory of communication. *The Bell System Technical Journal* **1948**, *27*, 379–423. doi:10.1002/j.1538-7305.1948.tb01338.x.
43. Hastie, T.; Friedman, J.; Tibshirani, R. *The Elements of Statistical Learning*; Springer New York, 2001. doi:10.1007/978-0-387-21606-5.
44. Peña, M.; Liao, R.; Brenning, A. Using spectrotemporal indices to improve the fruit-tree crop classification accuracy. *ISPRS Journal of Photogrammetry and Remote Sensing* **2017**, *128*, 158–169.
45. Bischl, B.; Richter, J.; Bossek, J.; Horn, D.; Thomas, J.; Lang, M. mlrMBO: A Modular Framework for Model-Based Optimization of Expensive Black-Box Functions. *ArXiv e-prints* **2017**, [1703.03373].
46. Binder, M.; Moosbauer, J.; Thomas, J.; Bischl, B. Multi-Objective Hyperparameter Tuning and Feature Selection using Filter Ensembles. *arXiv:1912.12912 [cs, stat]* **2020**, [arXiv:cs, stat/1912.12912].
47. Schratz, P.; Muenchow, J.; Iturriza, E.; Richter, J.; Brenning, A. Hyperparameter tuning and performance assessment of statistical and machine-learning algorithms using spatial data. *Ecological Modelling* **2019**, *406*, 109–120. doi:10/gf34bd.
48. Hutter, F.; Hoos, H.H.; Leyton-Brown, K. Sequential model-based optimization for general algorithm configuration. In *Lecture Notes in Computer Science*; Springer Berlin Heidelberg, 2011; pp. 507–523. doi:10.1007/978-3-642-25566-3\_40.
49. Jones, D.R.; Schonlau, M.; Welch, W.J. Efficient global optimization of expensive black-box functions. *Journal of Global Optimization* **1998**, *13*, 455–492. doi:10.1023/a:1008306431147.
50. Bergstra, J.; Bengio, Y. Random Search for Hyper-parameter Optimization. *J. Mach. Learn. Res.* **2012**, *13*, 281–305.
51. Brenning, A. Spatial cross-validation and bootstrap for the assessment of prediction rules in remote sensing: The R package sperrorest. 2012 IEEE International Geoscience and Remote Sensing Symposium. IEEE, 2012. R package version 2.1.0, doi:10.1109/igarss.2012.6352393.
52. Friedman, J.H. Greedy function approximation: A gradient boosting machine. *Annals of Statistics* **2001**, *29*, 1189–1232. doi:10.1214/aos/1013203451.
53. Greenwell, B.M.; Boehmke, B.C.; McCarthy, A.J. A Simple and Effective Model-Based Variable Importance Measure. *arXiv:1805.04755 [cs, stat]* **2018**, [arXiv:cs, stat/1805.04755].
54. Molnar, C. *Interpretable machine learning - A Guide for Making Black Box Models Explainable*; 2019.
55. Apley, D.W.; Zhu, J. Visualizing the Effects of Predictor Variables in Black Box Supervised Learning Models. *arXiv:1612.08468 [stat]* **2019**, [arXiv:stat/1612.08468].
56. R Core Team. *R: A Language and Environment for Statistical Computing*; 2019.
57. Chen, T.; Guestrin, C. XGBoost: A Scalable Tree Boosting System. Proceedings of the 22Nd ACM SIGKDD International Conference on Knowledge Discovery and Data Mining; ACM: New York, NY, USA, 2016; KDD '16, pp. 785–794. doi:10.1145/2939672.2939785.
58. Karatzoglou, A.; Smola, A.; Hornik, K.; Zeileis, A. kernlab – An S4 Package for Kernel Methods in R. *Journal of Statistical Software* **2004**, *11*, 1–20. doi:10.18637/jss.v011.i09.
59. Friedman, J.; Hastie, T.; Tibshirani, R. Regularization paths for generalized linear models via coordinate descent. *Journal of Statistical Software* **2010**, *33*, 1–22. doi:10.18637/jss.v033.i01.
60. Kurs, M.B. *praznik: Collection of Information-Based Feature Selection Filters*; 2018.
61. Zawadzki, Z.; Kosinski, M. *FSelectorRcpp: 'Rcpp' Implementation of 'FSelector' Entropy-Based Feature Selection Algorithms with a Sparse Matrix Support*; 2019.
62. Bischl, B.; Lang, M.; Kotthoff, L.; Schiffner, J.; Richter, J.; Studerus, E.; Casalicchio, G.; Jones, Z.M. mlr: Machine learning in R. *Journal of Machine Learning Research* **2016**, *17*, 1–5.
63. Landau, W.M. The drake R package: a pipeline toolkit for reproducibility and high-performance computing. *Journal of Open Source Software* **2018**, *3*.
64. Ghosh, M.; Adhikary, S.; Ghosh, K.K.; Sardar, A.; Begum, S.; Sarkar, R. Genetic algorithm based cancerous gene identification from microarray data using ensemble of filter methods. *Medical & Biological Engineering & Computing* **2019**, *57*, 159–176. doi:10.1007/s11517-018-1874-4.
65. Horler, D.N.H.; Dockray, M.; Barber, J. The red edge of plant leaf reflectance. *International Journal of Remote Sensing* **1983**, *4*, 273–288. doi:10.1080/01431168308948546.

66. Hais, M.; Hellebrandová, K.N.; Šrámek, V. Potential of Landsat spectral indices in regard to the detection of forest health changes due to drought effects. *Journal of Forest Science* **2019**, *65* (2019), 70–78. doi:10.17221/137/2018-JFS.
67. Gao, B.C. NDWI—A normalized difference water index for remote sensing of vegetation liquid water from space. *Remote Sensing of Environment* **1996**, *58*, 257–266. doi:10.1016/s0034-4257(96)00067-3.
68. Lehnert, L.W.; Meyer, H.; Bendix, J. *hsdar: Manage, analyse and simulate hyperspectral data in R*, 2016.
69. de Beurs, K.M.; Townsend, P.A. Estimating the effect of gypsy moth defoliation using MODIS. *Remote Sensing of Environment* **2008**, *112*, 3983–3990. doi:10/fpqhrc.
70. Rengarajan, R.; Schott, J.R. Modeling forest defoliation using simulated BRDF and assessing its effect on reflectance and sensor reaching radiance. Remote Sensing and Modeling of Ecosystems for Sustainability XIII. International Society for Optics and Photonics, 2016, Vol. 9975, p. 997503. doi:10.1117/12.2235391.
71. Meng, R.; Dennison, P.E.; Zhao, F.; Shendryk, I.; Rickert, A.; Hanavan, R.P.; Cook, B.D.; Serbin, S.P. Mapping canopy defoliation by herbivorous insects at the individual tree level using bi-temporal airborne imaging spectroscopy and LiDAR measurements. *Remote Sensing of Environment* **2018**, *215*, 170–183. doi:10/gd67bc.
72. Kälín, U.; Lang, N.; Hug, C.; Gessler, A.; Wegner, J.D. Defoliation estimation of forest trees from ground-level images. *Remote Sensing of Environment* **2019**, *223*, 143–153. doi:10/gf3wzz.
73. Goodbody, T.R.H.; Coops, N.C.; Hermosilla, T.; Tompalski, P.; McCartney, G.; MacLean, D.A. Digital aerial photogrammetry for assessing cumulative spruce budworm defoliation and enhancing forest inventories at a landscape-level. *ISPRS Journal of Photogrammetry and Remote Sensing* **2018**, *142*, 1–11. doi:10.1016/j.isprsjprs.2018.05.012.
74. Hlebarska, S.; Georgieva, M. Distribution of the invasive pathogen *Diplodia sapinea* on pinus spp. in Bulgaria. *Conference proceedings, 90 years forest research institute - for the society and nature, Sofia, Bulgaria, 24-26 October 2018* **2018**, pp. 61–70.
75. Kaya, A.G.A.; Yeltekin, Ş.; Lehtijarvi, T.D.; Lehtijarvi, A.; Woodward, S. Severity of *Diplodia* shoot blight (caused by *Diplodia sapinea*) was greatest on *Pinus sylvestris* and *Pinus nigra* in a plantation containing five pine species. *Phytopathologia Mediterranea* **2019**, *58*, 249–259.
76. Belgiu, M.; Drăguţ, L. Random forest in remote sensing: A review of applications and future directions. *ISPRS Journal of Photogrammetry and Remote Sensing* **2016**, *114*, 24–31. doi:10.1016/j.isprsjprs.2016.01.011.
77. Xia, J.; Liao, W.; Chanussot, J.; Du, P.; Song, G.; Philips, W. Improving Random Forest With Ensemble of Features and Semisupervised Feature Extraction. *IEEE Geoscience and Remote Sensing Letters* **2015**, *12*, 1471–1475. doi:10.1109/LGRS.2015.2409112.
78. Fassnacht, F.E.; Neumann, C.; Förster, M.; Buddenbaum, H.; Ghosh, A.; Clasen, A.; Joshi, P.K.; Koch, B. Comparison of Feature Reduction Algorithms for Classifying Tree Species With Hyperspectral Data on Three Central European Test Sites. *IEEE Journal of Selected Topics in Applied Earth Observations and Remote Sensing* **2014**, *7*, 2547–2561. doi:10.1109/JSTARS.2014.2329390.
79. Feng, J.; Jiao, L.; Liu, F.; Sun, T.; Zhang, X. Unsupervised feature selection based on maximum information and minimum redundancy for hyperspectral images. *Pattern Recognition* **2016**, *51*, 295–309. doi:10.1016/j.patcog.2015.08.018.
80. Georganos, S.; Grippa, T.; Vanhuysse, S.; Lennert, M.; Shimoni, M.; Kalogirou, S.; Wolff, E. Less is more: optimizing classification performance through feature selection in a very-high-resolution remote sensing object-based urban application. *GIScience & Remote Sensing* **2018**, *55*, 221–242. doi:10.1080/15481603.2017.1408892.
81. Rochac, J.F.R.; Zhang, N. Feature extraction in hyperspectral imaging using adaptive feature selection approach. 2016 Eighth International Conference on Advanced Computational Intelligence (ICACI), 2016, pp. 36–40. doi:10.1109/ICACI.2016.7449799.
82. Pal, M.; Foody, G.M. Feature Selection for Classification of Hyperspectral Data by SVM. *IEEE Transactions on Geoscience and Remote Sensing* **2010**, *48*, 2297–2307. doi:10.1109/TGRS.2009.2039484.
83. Keller, S.; Braun, A.C.; Hinz, S.; Weinmann, M. Investigation of the impact of dimensionality reduction and feature selection on the classification of hyperspectral EnMAP data. 2016 8th Workshop on Hyperspectral Image and Signal Processing: Evolution in Remote Sensing (WHISPERS), 2016, pp. 1–5. doi:10.1109/WHISPERS.2016.8071759.
84. Xu, S.; Zhao, Q.; Yin, K.; Zhang, F.; Liu, D.; Yang, G. Combining random forest and support vector machines for object-based rural-land-cover classification using high spatial resolution imagery. *Journal of Applied Remote Sensing* **2019**, *13*, 014521. doi:10.1117/1.JRS.13.014521.
85. Shendryk, I.; Broich, M.; Tulbure, M.G.; McGrath, A.; Keith, D.; Alexandrov, S.V. Mapping individual tree health using full-waveform airborne laser scans and imaging spectroscopy: A case study for a floodplain eucalypt forest. *Remote Sensing of Environment* **2016**, *187*, 202–217. doi:10/gf3wz4.
86. Ludwig, M.; Morgenthal, T.; Detsch, F.; Higginbottom, T.P.; Lezama Valdes, M.; Nauß, T.; Meyer, H. Machine learning and multi-sensor based modelling of woody vegetation in the Molopo Area, South Africa. *Remote Sensing of Environment* **2019**, *222*, 195–203. doi:10/gf3wz8.
87. Meyer, H.; Reudenbach, C.; Hengl, T.; Katurji, M.; Nauss, T. Improving performance of spatio-temporal machine learning models using forward feature selection and target-oriented validation. *Environmental Modelling & Software* **2018**, *101*, 1–9. doi:10.1016/j.envsoft.2017.12.001.
88. Zandler, H.; Brenning, A.; Samimi, C. Quantifying dwarf shrub biomass in an arid environment: comparing empirical methods in a high dimensional setting. *Remote Sensing of Environment* **2015**, *158*, 140–155. doi:10.1016/j.rse.2014.11.007.

89. Guo, Y.; Chung, F.L.; Li, G.; Zhang, L. Multi-Label Bioinformatics Data Classification With Ensemble Embedded Feature Selection. *IEEE Access* **2019**, *7*, 103863–103875. doi:10.1109/ACCESS.2019.2931035.
90. Radovic, M.; Ghalwash, M.; Filipovic, N.; Obradovic, Z. Minimum redundancy maximum relevance feature selection approach for temporal gene expression data. *BMC Bioinformatics* **2017**, *18*, 9. doi:10.1186/s12859-016-1423-9.
91. Vogelmann, J.E.; Rock, B.N.; Moss, D.M. Red edge spectral measurements from sugar maple leaves. *International Journal of Remote Sensing* **1993**, *14*, 1563–1575. doi:10.1080/01431169308953986.
92. Boochs, F.; Kupfer, G.; Dockter, K.; Kühbauch, W. Shape of the red edge as vitality indicator for plants. *International Journal of Remote Sensing* **1990**, *11*, 1741–1753. doi:10.1080/01431169008955127.
93. Nagler, P.L.; Inoue, Y.; Glenn, E.P.; Russ, A.L.; Daughtry, C.S.T. Cellulose absorption index (CAI) to quantify mixed soil–plant litter scenes. *Remote Sensing of Environment* **2003**, *87*, 310–325. doi:10.1016/j.rse.2003.06.001.
94. Walthall, C.L.; Daughtry, C.S.T.; Chappelle, E.W.; McMurtrey, J.E.; Kim, M.S. The Use of High Spectral Resolution Bands for Estimating Absorbed Photosynthetically Active Radiation (A Par) **1994**.
95. Carter, G.A. Ratios of leaf reflectances in narrow wavebands as indicators of plant stress. *International Journal of Remote Sensing* **1994**, *15*, 697–703. doi:10.1080/01431169408954109.
96. Zarco-Tejada, P.J.; Pushnik, J.C.; Dobrowski, S.; Ustin, S.L. Steady-state chlorophyll a fluorescence detection from canopy derivative reflectance and double-peak red-edge effects. *Remote Sensing of Environment* **2003**, *84*, 283–294. doi:10.1016/s0034-4257(02)00113-x.
97. Gitelson, A.A.; Gritz <sup>†</sup>, Y.; Merzlyak, M.N. Relationships between leaf chlorophyll content and spectral reflectance and algorithms for non-destructive chlorophyll assessment in higher plant leaves. *Journal of Plant Physiology* **2003**, *160*, 271–282. doi:10.1078/0176-1617-00887.
98. Oppelt, N.; Mauser, W. Hyperspectral monitoring of physiological parameters of wheat during a vegetation period using AVIS data. *International Journal of Remote Sensing* **2004**, *25*, 145–159. doi:10.1080/0143116031000115300.
99. Datt, B. Visible/near infrared reflectance and chlorophyll content in Eucalyptus leaves. *International Journal of Remote Sensing* **1999**, *20*, 2741–2759. doi:10.1080/014311699211778.
100. Datt, B. Remote Sensing of Chlorophyll a, Chlorophyll b, Chlorophyll a $\mathit{+}$ b, and Total Carotenoid Content in Eucalyptus Leaves. *Remote Sensing of Environment* **1998**, *66*, 111–121. doi:10.1016/s0034-4257(98)00046-7.
101. Datt, B. Remote Sensing of Water Content in Eucalyptus Leaves. *Australian Journal of Botany* **1999**, *47*, 909. doi:10.1071/bt98042.
102. le Maire, G.; François, C.; Dufrêne, E. Towards universal broad leaf chlorophyll indices using PROSPECT simulated database and hyperspectral reflectance measurements. *Remote Sensing of Environment* **2004**, *89*, 1–28. doi:10.1016/j.rse.2003.09.004.
103. Lemaire, G.; Francois, C.; Soudani, K.; Berveiller, D.; Pontailler, J.; Breda, N.; Genet, H.; Davi, H.; Dufrene, E. Calibration and validation of hyperspectral indices for the estimation of broadleaved forest leaf chlorophyll content, leaf mass per area, leaf area index and leaf canopy biomass. *Remote Sensing of Environment* **2008**, *112*, 3846–3864. doi:10.1016/j.rse.2008.06.005.
104. Apan, A.; Held, A.; Phinn, S.; Markley, J. Detecting sugarcane ‘orange rust’ disease using EO-1 Hyperion hyperspectral imagery. *International Journal of Remote Sensing* **2004**, *25*, 489–498. doi:10.1080/01431160310001618031.
105. Peñuelas, J.; Gamon, J.A.; Fredeen, A.L.; Merino, J.; Field, C.B. Reflectance indices associated with physiological changes in nitrogen- and water-limited sunflower leaves. *Remote Sensing of Environment* **1994**, *48*, 135–146. doi:10.1016/0034-4257(94)90136-8.
106. Huete, A. A comparison of vegetation indices over a global set of TM images for EOS-MODIS. *Remote Sensing of Environment* **1997**, *59*, 440–451. doi:10.1016/s0034-4257(96)00112-5.
107. Wu, W. The Generalized Difference Vegetation Index (GDVI) for Dryland Characterization. *Remote Sensing* **2014**, *6*, 1211–1233. doi:10.3390/rs6021211.
108. Smith, R.C.G.; Adams, J.; Stephens, D.J.; Hick, P.T. Forecasting wheat yield in a Mediterranean-type environment from the NOAA satellite. *Australian Journal of Agricultural Research* **1995**, *46*, 113. doi:10.1071/ar9950113.
109. Gitelson, A.A.; Buschmann, C.; Lichtenthaler, H.K. The Chlorophyll Fluorescence Ratio F735/F700 as an Accurate Measure of the Chlorophyll Content in Plants. *Remote Sensing of Environment* **1999**, *69*, 296–302. doi:10.1016/s0034-4257(99)00023-1.
110. Gitelson, A.A.; Kaufman, Y.J.; Merzlyak, M.N. Use of a green channel in remote sensing of global vegetation from EOS-MODIS. *Remote Sensing of Environment* **1996**, *58*, 289–298. doi:10.1016/s0034-4257(96)00072-7.
111. Galvão, L.S.; Formaggio, A.R.; Tisot, D.A. Discrimination of sugarcane varieties in Southeastern Brazil with EO-1 Hyperion data. *Remote Sensing of Environment* **2005**, *94*, 523–534. doi:10.1016/j.rse.2004.11.012.
112. Maccioni, A.; Agati, G.; Mazzinghi, P. New vegetation indices for remote measurement of chlorophylls based on leaf directional reflectance spectra. *Journal of Photochemistry and Photobiology B: Biology* **2001**, *61*, 52–61. doi:10.1016/s1011-1344(01)00145-2.
113. Daughtry, C. Estimating Corn Leaf Chlorophyll Concentration from Leaf and Canopy Reflectance. *Remote Sensing of Environment* **2000**, *74*, 229–239. doi:10.1016/s0034-4257(00)00113-9.
114. Wu, C.; Niu, Z.; Tang, Q.; Huang, W. Estimating chlorophyll content from hyperspectral vegetation indices: Modeling and validation. *Agricultural and Forest Meteorology* **2008**, *148*, 1230–1241. doi:10.1016/j.agrformet.2008.03.005.
115. Sims, D.A.; Gamon, J.A. Relationships between leaf pigment content and spectral reflectance across a wide range of species, leaf structures and developmental stages. *Remote Sensing of Environment* **2002**, *81*, 337–354. doi:10.1016/s0034-4257(02)00010-x.

116. Hernández-Clemente, R.; Navarro-Cerrillo, R.M.; Suárez, L.; Morales, F.; Zarco-Tejada, P.J. Assessing structural effects on PRI for stress detection in conifer forests. *Remote Sensing of Environment* **2011**, *115*, 2360–2375. doi:10.1016/j.rse.2011.04.036.
117. Qi, J.; Chehbouni, A.; Huete, A.R.; Kerr, Y.H.; Sorooshian, S. A modified soil adjusted vegetation index. *Remote Sensing of Environment* **1994**, *48*, 119–126. doi:10.1016/0034-4257(94)90134-1.
118. Hunt, E.; Rock, B. Detection of changes in leaf water content using Near- and Middle-Infrared reflectances. *Remote Sensing of Environment* **1989**, *30*, 43–54. doi:10.1016/0034-4257(89)90046-1.
119. Chen, J.M. Evaluation of vegetation indices and a Modified Simple Ratio for boreal applications. Technical report, Natural Resources Canada/ESS/Scientific and Technical Publishing Services, 1996. doi:10.4095/218303.
120. Dash, J.; Curran, P. Evaluation of the MERIS terrestrial chlorophyll index (MTCI). *Advances in Space Research* **2007**, *39*, 100–104. doi:10.1016/j.asr.2006.02.034.
121. Haboudane, D.; Miller, J.R.; Tremblay, N.; Zarco-Tejada, P.J.; Dextraze, L. Integrated narrow-band vegetation indices for prediction of crop chlorophyll content for application to precision agriculture. *Remote Sensing of Environment* **2002**, *81*, 416–426. doi:10.1016/S0034-4257(02)00018-4.
122. Serrano, L.; Peñuelas, J.; Ustin, S.L. Remote sensing of nitrogen and lignin in Mediterranean vegetation from AVIRIS data. *Remote Sensing of Environment* **2002**, *81*, 355–364. doi:10.1016/S0034-4257(02)00011-1.
123. Tucker, C.J. Red and photographic infrared linear combinations for monitoring vegetation. *Remote Sensing of Environment* **1979**, *8*, 127–150. doi:10.1016/0034-4257(79)90013-0.
124. Gitelson, A.; Merzlyak, M.N. Quantitative estimation of chlorophyll-a using reflectance spectra: Experiments with autumn chestnut and maple leaves. *Journal of Photochemistry and Photobiology B: Biology* **1994**, *22*, 247–252. doi:10.1016/1011-1344(93)06963-4.
125. Guanter, L.; Alonso, L.; Moreno, J. A method for the surface reflectance retrieval from PROBA/CHRIS data over land: application to ESA SPARC campaigns. *IEEE Transactions on Geoscience and Remote Sensing* **2005**, *43*, 2908–2917. doi:10.1109/tgrs.2005.857915.
126. Rondeaux, G.; Steven, M.; Baret, F. Optimization of soil-adjusted vegetation indices. *Remote Sensing of Environment* **1996**, *55*, 95–107. doi:10.1016/0034-4257(95)00186-7.
127. Chappelle, E.W.; Kim, M.S.; McMurtrey, J.E. Ratio analysis of reflectance spectra (RARS): An algorithm for the remote estimation of the concentrations of chlorophyll A, chlorophyll B, and carotenoids in soybean leaves. *Remote Sensing of Environment* **1992**, *39*, 239–247. doi:10.1016/0034-4257(92)90089-3.
128. Gamon, J.; Peñuelas, J.; Field, C. A narrow-waveband spectral index that tracks diurnal changes in photosynthetic efficiency. *Remote Sensing of Environment* **1992**, *41*, 35–44. doi:10.1016/0034-4257(92)90059-s.
129. Zarco-Tejada, P.; González-Dugo, V.; Williams, L.; Suárez, L.; Berni, J.; Goldhamer, D.; Fereres, E. A PRI-based water stress index combining structural and chlorophyll effects: Assessment using diurnal narrow-band airborne imagery and the CWSI thermal index. *Remote Sensing of Environment* **2013**, *138*, 38–50. doi:10.1016/j.rse.2013.07.024.
130. Garrity, S.R.; Eitel, J.U.; Vierling, L.A. Disentangling the relationships between plant pigments and the photochemical reflectance index reveals a new approach for remote estimation of carotenoid content. *Remote Sensing of Environment* **2011**, *115*, 628–635. doi:10.1016/j.rse.2010.10.007.
131. Merzlyak, M.N.; Gitelson, A.A.; Chivkunova, O.B.; Rakitin, V.Y. Non-destructive optical detection of pigment changes during leaf senescence and fruit ripening. *Physiologia Plantarum* **1999**, *106*, 135–141. doi:10.1034/j.1399-3054.1999.106119.x.
132. Blackburn, G.A. Quantifying chlorophylls and carotenoids at leaf and canopy scales. *Remote Sensing of Environment* **1998**, *66*, 273–285. doi:10.1016/S0034-4257(98)00059-5.
133. Penuelas, J.; Pinol, J.; Ogaya, R.; Filella, I. Estimation of plant water concentration by the reflectance Water Index WI (R900/R970). *International Journal of Remote Sensing* **1997**, *18*, 2869–2875. doi:10.1080/014311697217396.
134. Roujean, J.L.; Breon, F.M. Estimating PAR absorbed by vegetation from bidirectional reflectance measurements. *Remote Sensing of Environment* **1995**, *51*, 375–384. doi:10.1016/0034-4257(94)00114-3.
135. Cho, M.A.; Skidmore, A.K. A new technique for extracting the red edge position from hyperspectral data: The linear extrapolation method. *Remote Sensing of Environment* **2006**, *101*, 181–193. doi:10.1016/j.rse.2005.12.011.
136. Guyot, G.; Baret, F. Utilisation de la haute resolution spectrale pour suivre l'état des couverts végétaux. Spectral signatures of objects in remote sensing; Guyenne, T.D.; Hunt, J.J., Eds., 1988, Vol. 287, *ESA special publication*, p. 279.
137. Huete, A. A soil-adjusted vegetation index (SAVI). *Remote Sensing of Environment* **1988**, *25*, 295–309. doi:10.1016/0034-4257(88)90106-x.
138. Penuelas, J.; Filella, I.; Lloret, P.; Munoz, F.; Vilaleliu, M. Reflectance assessment of mite effects on apple trees. *International Journal of Remote Sensing* **1995**, *16*, 2727–2733. doi:10.1080/01431169508954588.
139. Vincini, M.; Frazzi, E.; D'Alessio, P. Angular dependence of maize and sugar beet VIs from directional CHRIS/Proba data. Proc. 4th ESA CHRIS PROBA workshop, 2006, Vol. 2006, pp. 19–21.
140. Jordan, C.F. Derivation of leaf-area index from quality of light on the forest floor. *Ecology* **1969**, *50*, 663–666. doi:10.2307/1936256.
141. Gitelson, A.A.; Merzlyak, M.N. Remote estimation of chlorophyll content in higher plant leaves. *International Journal of Remote Sensing* **1997**, *18*, 2691–2697. doi:10.1080/014311697217558.

142. McMurtrey, J.; Chappelle, E.; Kim, M.; Meisinger, J.; Corp, L. Distinguishing nitrogen fertilization levels in field corn (*Zea mays* L.) with actively induced fluorescence and passive reflectance measurements. *Remote Sensing of Environment* **1994**, *47*, 36–44. doi:10.1016/0034-4257(94)90125-2.
143. Zarco-Tejada, P.J.; Miller, J.R. Land cover mapping at BOREAS using red edge spectral parameters from CASI imagery. *Journal of Geophysical Research: Atmospheres* **1999**, *104*, 27921–27933. doi:10.1029/1999jd900161.
144. Lichtenthaler, H.; Lang, M.; Sowinska, M.; Heisel, F.; Miehe, J. Detection of vegetation stress via a new high resolution fluorescence imaging system. *Journal of Plant Physiology* **1996**, *148*, 599–612. doi:10.1016/s0176-1617(96)80081-2.
145. Hernández-Clemente, R.; Navarro-Cerrillo, R.M.; Zarco-Tejada, P.J. Carotenoid content estimation in a heterogeneous conifer forest using narrow-band indices and PROSPECTDART simulations. *Remote Sensing of Environment* **2012**, *127*, 298–315. doi:10.1016/j.rse.2012.09.014.
146. Elvidge, C.D.; Chen, Z. Comparison of broad-band and narrow-band red and near-infrared vegetation indices. *Remote Sensing of Environment* **1995**, *54*, 38–48. doi:10.1016/0034-4257(95)00132-k.
147. Filella, I.; Penuelas, J. The red edge position and shape as indicators of plant chlorophyll content, biomass and hydric status. *International Journal of Remote Sensing* **1994**, *15*, 1459–1470. doi:10.1080/01431169408954177.
148. Levin, N.; Kidron, G.J.; Ben-Dor, E. Surface properties of stabilizing coastal dunes: combining spectral and field analyses. *Sedimentology* **2007**, *54*, 771–788. doi:10.1111/j.1365-3091.2007.00859.x.
149. Lobell, D.B.; Asner, G.P.; Law, B.E.; Treuhaft, R.N. Subpixel canopy cover estimation of coniferous forests in Oregon using SWIR imaging spectrometry. *Journal of Geophysical Research: Atmospheres* **2001**, *106*, 5151–5160. doi:10.1029/2000jd900739.
150. Hunt, E.R.; Doraiswamy, P.C.; McMurtrey, J.E.; Daughtry, C.S.; Perry, E.M.; Akhmedov, B. A visible band index for remote sensing leaf chlorophyll content at the canopy scale. *International Journal of Applied Earth Observation and Geoinformation* **2013**, *21*, 103–112. doi:10.1016/j.jag.2012.07.020.
151. Broge, N.; Leblanc, E. Comparing prediction power and stability of broadband and hyperspectral vegetation indices for estimation of green leaf area index and canopy chlorophyll density. *Remote Sensing of Environment* **2001**, *76*, 156–172. doi:10.1016/s0034-4257(00)00197-8.

## Short Biography of Authors



**Patrick Schratz** is a Data Scientist working in Zurich, Switzerland. His area of expertise is applied machine learning, more specifically the field of environmental modeling. He is a PhD candidate in geographic information science in the Department of Geography at Friedrich Schiller University Jena where he conducts research in environmental modeling. At cynkra GmbH in Zurich, Patrick is an R consultant with many years of experience in the following fields: CI/CD, package development, DevOps tasks, machine learning and spatio-temporal data handling.



**Jannes Muenchow** is a GIScientist working in tropical ecology since 2007 with a special interest in ENSO, biodiversity, species distribution modeling and predictive mapping. He received his PhD from Friedrich-Alexander University Erlangen-Nürnberg (Germany) in 2013. He joined the business location department of a large consulting company as a geo-data scientist for more than two years until the prediction of a strong El Niño event brought him back to academia in 2016 (Friedrich Schiller University Jena). Currently, his research focuses on developing open source tools for ecology, geomorphology and qualitative GIS. He is a co-author of the book "Geocomputation with R".



**Eugenia Iturrutxa** received the Ecology and Ph.D degree in Plant Protection from the University of the Basque Country in 2001. Since 1999 her main research has focused on forest health, on the study of diverse species of native and introduced pathogenic fungi in forests and forest plantations. Her research the NEIKER research center includes the distribution of diseases, analysis of predisposing factors for them, genetic and phenotypic studies of populations and their epidemiology.



**José Cortés** received his B.S. in Mathematics and M.S. in Statistics from Arizona State University, Arizona, USA, in 2014 and 2016, respectively. Currently he is a PhD student at Friedrich Schiller University, Jena, Germany. He is a member of the International Max Planck Research School on Global Biogeochemical Cycles (IMPRS-gBGC), a joint program with the Max Planck Institute for Biogeochemistry. His research focuses on spatio-temporal trend detection in environmental data.



**Bernd Bischl** obtained his Ph.D from Dortmund Technical University in 2013. He is a professor of Statistical Learning and Data Science in the Department of Statistics at Ludwig-Maximilians-Universität in Munich, Germany, and a director of the Munich Center for Machine Learning. His research interests include AutoML, model selection, interpretable ML and XAI.



**Alexander Brenning** (Ph.D. 2005) graduated in mathematics at Technical University of Freiberg, Germany, and received his Ph.D. in geography from Humboldt-Universität zu Berlin. He served as an assistant professor and tenured associate professor in geomatics at the University of Waterloo, Ontario, Canada from 2007 until 2015, when he was appointed as a full professor in geographic information science at Friedrich Schiller University Jena, Germany. Dr. Brenning's research interests include statistical and machine-learning techniques for environmental modeling and remote sensing. He has also contributed to open-source geocomputation by developing R packages for spatial cross-validation and GIS coupling.